$E801748$

②

AFATL-TR-88-101

A Displacement Pattern Matching Application in Elastic-Plastic Hybrid Stress Analysis

JIM SIRKUS

DEPARTMENT OF AEROSPACE MECHANICS
ENGINEERING SCIENCE
GAINESVILLE, FL 32611

AUGUST 1988

FINAL REPORT FOR PERIOD JUNE 1987 - MAY 1988

DTIC
ELECTE
SEP 1 5 1988

H

APPROVED FOR PUBLIC RELEASE; DISTRIBUTION UNLIMITED

AIR FORCE ARMAMENT LABORATORY
Air Force Systems Command ∎ United States Air Force ∎ Eglin Air Force Base, Florida

88 9 15

REPORT DOCUMENTATION PAGE		Form Approved OMB No. 0704-0188

1a. REPORT SECURITY CLASSIFICATION UNCLASSIFIED	1b. RESTRICTIVE MARKINGS
2a. SECURITY CLASSIFICATION AUTHORITY	3. DISTRIBUTION / AVAILABILITY OF REPORT Approved for public release; distribution is unlimited.
2b. DECLASSIFICATION / DOWNGRADING SCHEDULE	
4. PERFORMING ORGANIZATION REPORT NUMBER(S)	5. MONITORING ORGANIZATION REPORT NUMBER(S) AFATL-TR-88-101

6a. NAME OF PERFORMING ORGANIZATION University of Florida	6b. OFFICE SYMBOL (If applicable)	7a. NAME OF MONITORING ORGANIZATION Warheads Branch Munitions Division
6c. ADDRESS (City, State, and ZIP Code) Department of Aerospace Mechanics Engineering Science Gainesville FL 32611		7b. ADDRESS (City, State, and ZIP Code) Air Force Armament Laboratory Eglin AFB FL 32542-5434

8a. NAME OF FUNDING / SPONSORING ORGANIZATION Air Force Office of Scientific & Research	8b. OFFICE SYMBOL (If applicable) AFOSR	9. PROCUREMENT INSTRUMENT IDENTIFICATION NUMBER AFOSR F49620-85-C-00131 SB 5851-0360
8c. ADDRESS (City, State, and ZIP Code)		10. SOURCE OF FUNDING NUMBERS

PROGRAM ELEMENT NO.	PROJECT NO.	TASK NO	WORK UNIT ACCESSION NO
FUNDED BY AFOSR 6.1 FUNDS			

11. TITLE (Include Security Classification)
A Displacement Pattern Matching Application in Elastic-Plastic Hybrid Stress Analysis

12. PERSONAL AUTHOR(S) Jim Sirkus

13a. TYPE OF REPORT Final	13b. TIME COVERED FROM Jun 87 TO May 88	14. DATE OF REPORT (Year, Month, Day)	15. PAGE COUNT 119

16. SUPPLEMENTARY NOTATION Report is in contractor format. Availability of report is specified on verso of front cover. This TR was published as a thesis and an open journal. Therefore, the AFATL format was not used.

17.	COSATI CODES		18. SUBJECT TERMS (Continue on reverse if necessary and identify by block number)
FIELD	GROUP	SUB-GROUP	Boundary Element Method, Plasticity

19. ABSTRACT (Continue on reverse if necessary and identify by block number) A two-dimensional hybrid experimental-numerical technique for elastic-plastic stress analysis is presented. This technique results from merging two relatively new technologies in engineering mechanics: boundary element methods and image processing. A syntactic pattern recognition scheme termed "Displacement Pattern Matching" (DPM) determines displacement boundary conditions to be used in an elastic-plastic boundary element (EPBEM) code. The result is an automated stress analysis tool. Displacement pattern matching is a process where displacements are measured by tracking an arbitrary array of "black" spots on a "white" specimen are compared in a double exposure format to determine displacements. Displacement pattern matching is a full-field technique, with spatial resolution on the order of .0001 inch. Displacement pattern matching supplies the actual specimen displacement increments to the von Mises, isotropic work hardening, boundary element code. Given these displacements and free surface conditions, EPBEM is able to incrementally calculate the internal state of stress at selected locations. Results obtained for a variety of geometries and loading conditions compared well with ANSYS finite element and selected published experimental solutions and therefore are encouraging.

20. DISTRIBUTION / AVAILABILITY OF ABSTRACT ☐ UNCLASSIFIED/UNLIMITED ☒ SAME AS RPT. ☐ DTIC USERS	21. ABSTRACT SECURITY CLASSIFICATION Unclassified
22a. NAME OF RESPONSIBLE INDIVIDUAL Michael E. Gunger	22b. TELEPHONE (Include Area Code) 904-882-2145	22c. OFFICE SYMBOL AFATL/MNW

DD Form 1473, JUN 86   Previous editions are obsolete.   SECURITY CLASSIFICATION OF THIS PAGE

PREFACE

This report describes the work performed by Jim Sirkis and Chuck Taylor at the University of Florida, under Air Force Office of Scientific Research (AFOSR) "Research Initiation Program," Contract No. F49620-85-C-0013/SB5851-0360, Subcontract No. S-760-6MG-142. This research was conducted at the Department of Aerospace Engineering, Mechanics and Engineering Science, University of Florida, Gainesville during the period June 1, 1987 through May 31, 1988.

The author would like to acknowledge the support of Air Force Systems Command and AFOSR for their support in this effort. The author would also like to thank the Clusters and Warheads Branch (MNW) at the Air Force Armament Laboratory (AFATL) for their support and cooperation during this research period.

TABLE OF CONTENTS

LIST OF FIGURES

LIST OF FIGURES (CONCLUDED)

SECTION I

INTRODUCTION

Substantiating postulations through experimentation, or using experimentation to draw new conclusions, is fundamental to science and engineering. This service is provided to theoretical mechanics by the field of experimental mechanics. Before coming to any conclusions, experimentalists demand confidence in their work; as a result, many time consuming experiments are repeated just to be sure. Experimental stress analysis is no different. Repeating experimental procedures, often including more than one technique, is the norm when searching for the solution to engineering problems [1]. The tedious nature of manual data extraction and reduction led researchers to explore automated extraction and reduction schemes. Hence, hybrid experimental-numerical stress analysis techniques evolved.

The shear difference method [2] is an early example of an experimental-numerical hybrid method in stress analysis. Since then, researchers have acknowledged the need for

improved and more encompassing hybrid techniques [3]. Prior to the development of digital image processing, most hybrid stress analysis techniques suffered from the need for manual data extraction. Seguci et al. [4] bridged the gap between computer analysis and experimental data via a digitized video picture. Their paper marks the beginning of the era where researchers started using digital image processing techniques with structural analysis codes to produce viable stress analysis techniques [5-6]. During this same era, researchers started to exploit a new numerical structural analysis technique, the boundary element method.

The appearance of boundary element methods (BEM) was coincident with the advent of digital computers [7], but they did not become popular until Rizzo [8] introduced the direct boundary element method. Still, BEM (sometimes called boundary integral equation methods) have yet to achieve the acceptance of finite element methods (FEM). The reluctance of the technical community to embrace BEM is largely attributable to its less familiar mathematical foundations [9]. However, in the past ten years, the popularity of BEM for hybrid and purely numerical studies has greatly increased.

Moslehy and Ranson [10], Umeagukwu et al. [11], and Balas et al. [12] introduced early BEM-experimental hybrid techniques, but all require manual data extraction. Liu [13] introduced a hybrid method using digital image

processing and elastic BEM. In his method, digital image correlation is used to find displacements interior to the boundary. Liu then solves the inverse boundary element problem to find the boundary conditions. Liu's work finally relieved the experimenter of data extraction responsibilities.

Hybrid elastic boundary element-experimental methods are presently an important research area [14-15]. Equally important are elastic-plastic boundary element-experimental methods, but there seems to be an absence of research in this topic. Elastic-plastic boundary element methods (EPBEM) were first conceived by Swedlow and Cruse [16] in 1971 and then implemented by Riccardella [17] in 1973. Since then, EPBEM have grown in popularity. Telles [18] gives an excellent historical review of the development of this numerical method. The rapid increase in the popularity of elastic-plastic boundary element is due to [18-19]:

1. The BEM solution reduces much of the domain by one dimension. That is, in elastic regions, only the boundary is discretized.

2. Only the plastic zone must be domain discretized.

3. BEM produces a reduced set of equations (compared with FEM).

4. The user preparation to run the codes is greatly reduced.

5. Expertise requirements are greatly reduced from techniques dependent on mesh generation.

6. Infinite and semi-infinite problems can be accurately and efficiently modelled.

7. The displacements, stresses and strains can be selectively calculated.

8. EPBEM affords a high degree of accuracy.

The EPBEM algorithm used here is conceptually equivalent to the rate form of elastic BEM with a body force [20]. The governing differential equation for displacements can be arranged so that the homogeneous part is the Navier equation for total displacement rates. The nonhomogeneous part contains the nonlinear terms associated with spatial derivatives of the plastic strain rate. These nonlinear terms constitute a pseudo body force. The boundary element solution approach leads to an equation for the unknown boundary conditions in terms of the known boundary conditions (assuming the body forces are known). Since the plastic strain rates introduce an additional set of unknowns, the boundary element method requires an additional set of equations. The constitutive model provides enough information so that an initial strain [21] solution procedure can be successful. This EPBEM algorithm uses the isotropic hardening, von Mises yield criterion discussed by Swedlow [22].

In the natural progression of coupling boundary element methods and image processing techniques, this report introduces a two-dimensional experimental EPBEM technique. The experimental technique used here, displacement pattern matching, is a spinoff of the pattern mapping technique, first introduced by Fail [23]. Pattern mapping uses digital image processing and syntactic pattern recognition techniques to discern the motion of spots applied to a specimen. The history of pattern mapping can be traced through the photogrid method [24-25] and the fine-grid method [26-27]. These predecessors measured strain by measuring the local motion of large grids of dots applied to a model. Typically, the measurements were made by the experimenter and thus subject to a large degree of error. Kawasaki et al. [28] automated the fine grid method to attain good accuracy, but the equipment is necessarily complex and dedicated to the fine grid task.
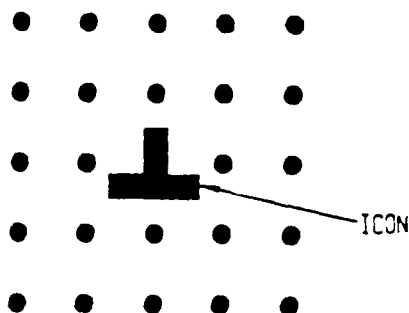
Figure 1. Five-by-five pattern mapping grid with an icon.

Pattern mapping has the advantage of using general purpose image processing hardware. Additionally, a regular grid need not cover the entire specimen. In pattern mapping, one places an arbitrarily shaped matrix of spots (for example a 5x5 square) at the locations in which the displacements and strains are required (Figure 1). Located in this matrix, there is a special spot (termed an Icon) that serves as a reference spot for determining the relative locations of the individual spots and the matrix orientation. The position of each spot in the matrix is then recorded before and after motion. Differencing yields the displacement, and a strain definition (small, large, Lagrangian, etc.) provides a measure of strain [23]. In the proposed hybrid stress analysis, only the displacement is required, thus the name "displacement pattern matching" (DPM). This requirement further relaxes the grid geometry restrictions to only placing a spot at the locations where one desires the displacements. In addition, DPM does not use an Icon, resulting in the reduction of the syntactic recognition language from context sensitive to context free. The combination of displacement pattern matching for data extraction and elastic-plastic boundary element methods for structural analysis leads to a fully automated technique for measuring plastic stress and strain.

Three experiments explore the ability of the automated
hybrid technique as a nondestructive stress analysis tool.
All are plane stress tests of 1100-H14 aluminum, using an MTS
testing machine to apply controlled loads. The first is a
simple uniaxial stress test of a thin sheet. The second is
the investigation of a thin sheet with a central hole,
subject to uniform end loads (perforated strip tension
test); and the third is a thin V-notched sheet, subject to
uniform end loads (notched tension specimen test). All
three experiments serve to show the usefulness of this
hybrid DPM-EPBEM technique in elastic-plastic stress
analysis.

SECTION II

THE ELASTIC-PLASTIC BOUNDARY ELEMENT METHOD

II.1 Linear Elastic BEM

The derivation of the two-dimensional integral equations governing linear elasticity and their solutions provide an entry point to the understanding of the underlying concepts of boundary element methods. The elasticity equations and solutions are first derived, and then they are extended to include plastic flow. The basic assumptions in the development are

> 1) The problem is well posed (proper boundary conditions are specified).
>
> 2) The material is isotropic and linear elastic.
>
> 3) Small displacement theory is applicable.

Elastic boundary element methods are based on the numerical solution of the integral equations governing the deformation in an elastic solid. These integral equations

can be derived by starting with the following form of the virtual work statement:

$$\int_{\Gamma} t_i^*(s) u_i(s) d\Gamma + \int_{\Omega} b_i^*(p) u_i(p) d\Omega = \int_{\Omega} \sigma_{ij}^*(s,p) \epsilon_{ij}(p) d\Omega; \qquad (II-1)$$

where t_i, u_i, and b_i denote the traction, displacement and body force vectors respectively. The stress tensor is σ_{ij} and the strain tensor is ϵ_{ij}. The differential $d\Gamma$ is an element on the bounding curve and the differential $d\Omega$ is an interior surface element. Also, the *-superscript denotes an arbitrary equilibrium set and no superscript denotes an arbitrary compatible set [29]. The right hand side of Equation (II-1) can be rewritten using an identical form of virtual work but with the significance of the superscript and no superscript interchanged. The resulting equation, given below, is:

$$\int_{\Gamma} t_i^*(s) u_i(s) d\Gamma + \int_{\Omega} b_i^*(p) u_i(p) d\Omega = \int_{\Gamma} t_i(s) u_i^*(s) d\Gamma$$

$$+ \int_{\Omega} b_i(p) u_i^*(p) d\Omega \qquad (II-2)$$

This equation is known as Betti's Second Reciprocal Theorem [18]. In these two equations, s represents a point on the bounding curve and p represents a point in the interior.

Since the choice is arbitrary, u_i, t_i, and b_i are chosen as the traction, displacement, and body force of the true body. The choice of the *-superscript set is also arbitrary; therefore, it is chosen as Kelvin's solution to the response of an infinite, two-dimensional, elastic medium which is subjected to arbitrarily located, mutually orthogonal point loads. Kelvin's solution is found by using the Green's function approach of letting b_i^* be the two-dimensional Dirac delta function $\delta_{ij}P_j(p)$ [30]; where $P_j(p)$ (for j=1,2) are two mutually orthogonal unit loads (i=1,2). This designation is substituted into the adjoint form of the Navier equation to yield the following forms of displacement, traction, stress and strain:

$$u_i^*(s) = U_{ij}^*(s,p)P_j(p),$$
$$t_i^*(s) = T_{ij}^*(s,p)P_j(p),$$
$$\epsilon_{ki}^*(p) = E_{jki}^*(s,p)P_j(p), \text{ and} \qquad (II-3)$$
$$\sigma_{ki}^*(p) = S_{jki}^*(s,p)P_j(p);$$

where

$$U_{ij}^* (s,p) = \frac{-1}{8\pi(1-\nu)G} ((3-4\nu)\ln(r)\,\delta_{ij} - r_{,i}r_{,j}),$$

$$T_{ij}^* (s,p) = \frac{-1}{4\pi(1-\nu)G} \{[(1-2\nu)\delta_{ij}+2r_{,i}r_{,j}]\frac{dr}{dn}$$

$$- (1-2\nu)[r_{,i}n_j - r_{,j}n_i]\},$$

$$E^*_{jki}(s,p) = \frac{-1}{8\pi(1-\nu)Gr}\,\{(1-2\nu)(r,_k\delta_{ij}+r,_j\delta_{ik})$$

$$-\,r,_i\delta_{jk}+2r,_ir,_jr,_k\},$$

$$(II-4)$$

$$S^*_{jki}(s,p) = \frac{-1}{4\pi(1-\nu)r}\,\{(1-2\nu)(r,_k\delta_{ij}+r,_j\delta_{ki}-r,_i\delta_{jk})$$

$$+\,2r,_ir,_jr,_k\};$$

In Equations (II-4), $r^2 = (X_p-X_s)^2 +(Y_p-Y_s)^2$, ν is Poisson's ratio, n_i is the outward normal vector to the bounding surface, dr/dn is the normal derivative, and G is the shear modulus. The function $U^*_{ij}(s,p)$ is known as Kelvin's fundamental solution; where $T^*_{ij}(s,p)$, $E^*_{jki}(s,p)$, and $S^*_{jki}(s,p)$ are the traction, strain, and stress respectively that are associated with the fundamental solution. Sokolnikoff [31] provides a detailed development of U^*_{ij} and most boundary element texts include a derivation of T^*_{ij}, E^*_{jki}, and S^*_{jki} (for example see Ref. [20]).

Somigliano's Identity for displacements [32] is the basis for the boundary element method. This identity is found by substituting the fundamental solution into Betti's Second Reciprocal Theorem.

$$u_i(p) = \int_\Gamma U^*_{ij}(s,p)t_j(s)d\Gamma - \int_\Gamma T^*_{ij}(s,p)u_j(s)d\Gamma$$

$$+ \int_\Omega U^*_{ij}(s)b_j(p)d\Omega. \qquad (II-5)$$

Equation (II-5) can be restated as, given all the boundary

conditions (the body force is always considered known),

information at any point inside the boundary is attainable

without finding the entire domain solution. In other words,

selective calculation of interior displacements is possible

by a line integral around the bounding curve. An

appropriate real estate analogy is that a buyer need never

see the property, he only needs to walk the perimeter to

know every detail of the lot and the house. This is a truly

remarkable statement. The solution to Navier's equation is

reduced in dimension (in the sense that only the boundary

must be examined). The reduced dimensionality (surface to

line integral) makes BEM a very attractive numerical

solution technique. But still, the unknown boundary

conditions remain unknown, so the solution is not yet

tractable.

The above dilemma is easily remedied by taking the

limit of Equation (II-5) as the field point, p, approaches

the surface [8]. Mathematically stated as

$$\text{Lim } u_i(p), \quad \text{where} \quad \ell \text{ is a point on } \Gamma. \qquad \text{(II-6)}$$
$$p \to \ell$$

Since somewhere on the boundary $r=0$ ($\ell=s$), and since

$T^*_{ij}(s,p)$ is proportional to $1/r$ and U^*_{ij} is proportional to

$\ln(r)$, the limit in Equation (II-6) produces a singular

integral. This singular integral exists [8] and is

interpreted in the principal value sense [33]. The

existence proof of the limit in Equation (II-6) follows by segmenting the integration path to isolate the singular point, then taking the limit of the integral as the singular integration path shrinks to zero.

The existence of the right hand side's second integral in Equation (II-5) is verified by the approach described above. Using the notation in Figure 2,

$$\lim_{\rho \to 0} \int_\Gamma T^*_{ij}(s,\ell) u_j(s) d\Gamma = \lim_{\rho \to 0} \int_\Gamma T^*_{ij}(s,\ell) u_j(s) d\Gamma$$

$$+ \lim_{\rho \to 0} \int_{\Gamma - \Gamma'} T^*_{ij}(s,\ell) u_j G d\Gamma' . \tag{II-7}$$

The first integral on the right hand side of Equation (II-7) exists in the ordinary sense but the integral around the singular circuit must be viewed carefully. The singular integral's existence is confirmed by making the following two substitutions:

1) $T^*_{ij} = g(\theta)/\rho$; where $g(\theta)$ is order one and 2) $d\Gamma = \rho d\theta$

$$\lim_{\rho \to 0} \int_{\theta_1}^{\theta_2} g(\theta) d\theta = \int_{\theta_1}^{\theta_2} g(\theta) \ d\theta . \tag{II-8}$$

Generally, the limit in equation (II-7) is not evaluated until assumptions about the interpolation of u_j over the boundary Γ are made (see section III. 4). Lachat [34], following closely the arguments of

SINGULAR POINT
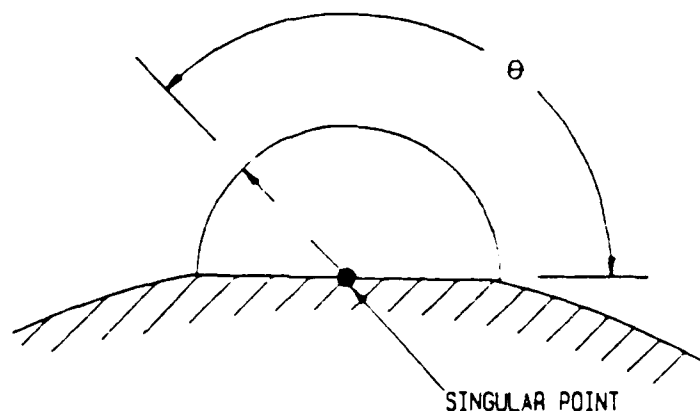
Figure 2. Circuit around the singularity.

Muskhelishvili [33], showed that Equation (II-7) evaluates to $C_{ij}u_j$ regardless of the interpolation function. In the strict sense C_{ij} is a constant and is dependent on surface smoothness; but in the numerical solution, C_{ij} is also dependent on the interpolation function.

The same arguments hold for the other two integrals on the right hand side of Equation (II-5). In the first integral U^*_{ij} is proportional to $\ln(\rho)$ and in the third integral the area element is $\rho\,d\rho\,d\phi$. In both cases, the limit evaluates to zero. Assembling the aforementioned results yields the boundary element constraint equation.

$$C_{ij}(s)u_j(s) + \int_\Gamma T^*_{ij}(s,\ell)u_j(s)\,d\Gamma = \int_\Gamma U^*_{ij}(s,\ell)t_j(s)\,d\Gamma$$

$$(II-9)$$

$$+ \int_\Omega U^*_{ij}(s,p)b_j(p)\,d\Omega.$$

For a well posed problem, Equation (II-9) provides the unknown boundary conditions. These boundary conditions, in turn, can be used in Equation (II-5) to give the displacement at any desired interior point. As an example, if the surface traction is prescribed on the surface, then Equation (II-9) yields the unknown surface displacements. Then Equation (II-5) gives the displacement solution in the domain. This procedure is valid for prescribed tractions, prescribed displacements, or mixed boundary conditions.

II.2 Elastic-Plastic BEM

The governing equations in elastic-plastic boundary element methods are developed along the same lines as elastic BEM; the main difference is the idea of initial strain. This section will describe the initial strain concept and its effect on the BEM development. Additionally, the need for a second equation is illustrated and a plastic flow rule is introduced to meet that need.

Swedlow and Cruse [16] were first to formulate the initial strain boundary element theory. Since then, Riccardella [17], Mendelson and Albers [35], Mukherjee [36], Telles [18] and others have developed initial strain algorithms to solve engineering problems. Although initial strain theory is not restricted to a particular flow rule, it will be described in the context of isotropic work

hardening and incremental plasticity. In accordance with accepted terminology and notation, rate and increment will be used interchangeably and superior dots denote time differentiation.

In an elastic-plastic body, strains can be categorized as either elastic or plastic. In initial strain EPBEM, the plastic strain is assumed to act as a residual strain; each load increment is just a deviation from that residual strain. The adjective "residual" refers to the idea that the solid knows, by some internal mechanism, the plastic strain increment before the application of the load increment. When the increment is applied, the material only deforms elastically. Loosely interpreted, the initial strain concept states that plastic deformation occurs before elastic deformation. This idea of initial strain is analogous to Martin's discussion of convergence by the superposition of elastic and residual stresses [37]. As an aside, initial strain has little meaning in finite strain plasticity since numerically, this is a load and unload process. Initial strain, however, is acceptable in incremental plasticity.

The derivation of the integral equations governing elastic-plastic BEM follow the same procedure outlined in Section II.1. This time, however, the starting point is a rate form of virtual work:

$$\int_\Gamma t_i^*(s)\dot{u}_i(s)\,d\Gamma + \int_\Omega b_i^*(p)\dot{u}_i(p)\,d\Omega = \int_\Omega \sigma_{ij}^*(s,p)\dot{\epsilon}_{ij}(p)\,d\Omega; \qquad \text{(II-10)}$$

The superior dot denotes time differentiation, the terms designated by the *-superscript denote an arbitrary equilibrium set, and the terms with no superscript denote an arbitrary compatible set. The total strain tensor can be decomposed into elastic and plastic parts; thereby, rewriting Equation (II-10) as

$$\int_\Gamma t_i^*(s)\dot{u}_i(s)\,d\Gamma + \int_\Omega b_i^*(p)\dot{u}_i(p)\,d\Omega = \int_\Omega \sigma_{ij}^*(s,p)\dot{\epsilon}_{ij}^p(p)\,d\Omega$$
$$+ \int_\Omega \sigma_{ij}^*(s,p)\dot{\epsilon}_{ij}^e(p)\,d\Omega. \qquad \text{(II-11)}$$

During each load increment <u>both</u> elastic and plastic deformation are present. Even though plastic deformation occurs, the stress rate is still related to the elastic strain rate by Hooke's law [38]. Accordingly, the stress rate can be found by isolating the elastic part of the total strain increment and using Hooke's Law:

$$\dot{\sigma}_{ij} = 2G(\dot{\epsilon}_{ij} - \dot{\epsilon}_{ij}^p) + \frac{2G\nu}{1-2\nu}(\dot{\epsilon}_{kk} - \dot{\epsilon}_{kk}^p). \qquad \text{(II-12)}$$

Equation (II-12) allows the following substitution to be made in equation (II-11): $\sigma_{ij}^* \dot{\epsilon}_{ij}^e = \epsilon_{ij}^* \dot{\sigma}_{ij}$.

Equation (II-11) can then be written in a form similar to

Equation (II-2) by applying the rate form of virtual work
(with the significance of the superscripts interchanged)
to the $\epsilon_{ij}^{*}\dot{\sigma}_{ij}$ term;

$$\int_{\Gamma} t_i^{*}(s)\dot{u}_i(s)\,d\Gamma \;-\; \int_{\Gamma}\dot{t}_i(s)u_i^{*}(s)\,d\Gamma \;+\; \int_{\Omega} b_i^{*}(p)\dot{u}_i(p)\,d\Omega$$

$$-\int_{\Omega}\dot{b}_i(p)u_i^{*}(p)\,d\Omega \;=\; \int_{\Omega}\sigma_{ij}^{*}(s,p)\dot{\epsilon}_{ij}^{p}(p)\,d\Omega.$$

(II-13)

The difference between this integral equation and
Equation (II-2) is the integral which includes the plastic
strain rate term. As in Section II.1, the terms with the
*-superscript are chosen as Kelvin's solution.
(Equation (II-3)) and the terms with no superscript are
chosen as the displacement rate, traction rate, body force
rate and strain rate of the true body. These designations
lead to Somligliano's Identity for inelastic materials;

$$\dot{u}_j(s) \;=\; \int_{\Gamma} U_{ij}^{*}(s,p)\dot{t}_i(s)\,d\Gamma \;-\; \int_{\Gamma} T_{ij}^{*}(s,p)\dot{u}_i(s)\,d\Gamma \;+$$

$$\int_{\Gamma} U_{ij}^{*}(s,p)\dot{b}_i(p)\,d\Omega \;+\; \int_{\Omega}\sigma_{ij}^{*}(s,p)\dot{\epsilon}_{ij}^{p}(p)\,d\Omega.$$

(II-14)

The limiting process to find the elastic-plastic boundary
element constraint equation is identical to that described
in Section II.1. The plastic strain rate integral exists
and has no contribution to C_{ij}.

$$C_{ij}(s) \; \dot{u}_j(s) \; + \; \int_\Omega T^*_{ij}(s,\ell)\dot{u}_i(\ell)d\Gamma \; = \; \int_\Omega U^*_{ij}(s,\ell) \; \dot{t}_i(\ell)d\Gamma$$

$$+ \; \int_\Gamma U^*_{ij}(s,\ell)\dot{b}_i(\ell)d\Omega \; + \; \int_\Gamma S^*_{jki}(s,\ell)\dot{\varepsilon}^p_{ki}(\ell)d\Omega;$$

(II-15)

where $\sigma^*_{ki}(s,p) = S^*_{jki}(s,p)P_j(p)$ is used.

If the plastic strain is known apriori and if the problem is well posed, then Equation (II-15) yields the unknown boundary conditions. The boundary information could then be used to find the displacements in an elastic-plastic solid (Equation (II-14)). The problem here is that prior knowledge of the plastic strain rate is just an idealization of the initial strain solution approach. In reality, the plastic strain rate is an unknown quantity; therefore, an additional relation is needed.

II.3 Elastic-Plastic Flow Rule

An isotropic work hardening, von Mises flow rule is introduced to satisfy the above requirement for an additional relation. Although a multitude of flow rules have been proposed [39], an isotropic work hardening flow rule provides an easily understood constitutive model. It also provides a reasonable approximation to material response while loading takes place. However, one should be aware that the von Mises yield criterion is limited in that it does not provide for hysteresis [40].
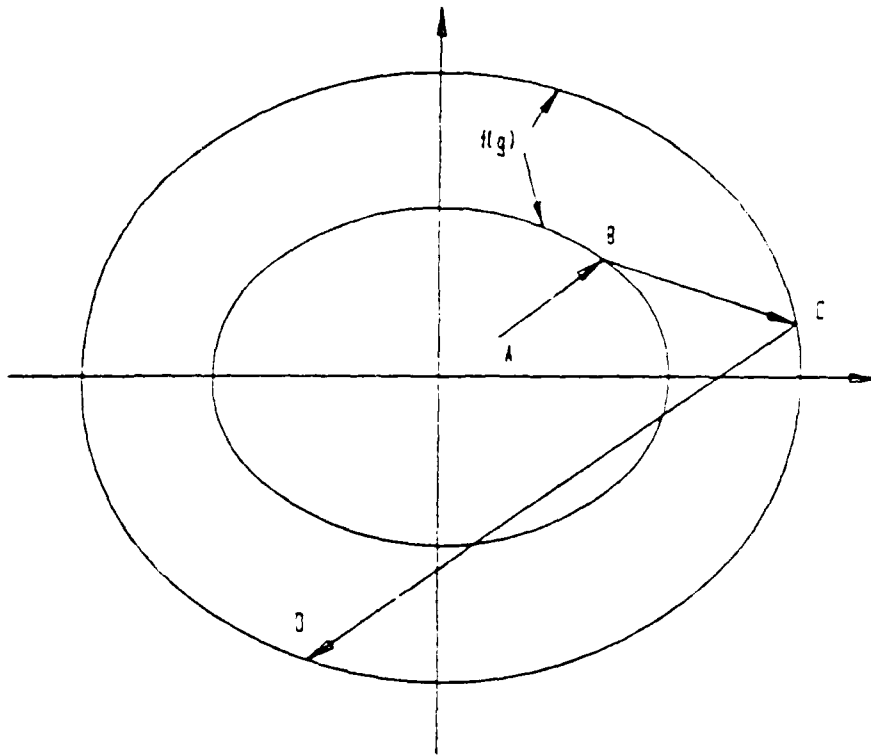
Figure 3. Isotropic hardening yield surface.

The yield function of an isotropic hardening material mathematically describes a yield surface that maintains its shape but increases in size as a function of the plastic deformation. As an example (Figure 3), f(g) defines the yield surface, where g is some measure of plastic deformation. The loading path AB is purely elastic, where B

is an infinitesimal amount inside the yield surface. As the
solid is loaded along BC, plastic deformation commences and
the yield surface expands. Now, unloading along CD is
purely elastic until D is reached. As a result, the elastic
domain is enlarged.

There are infinitely many forms of isotropic work
hardening to choose from; Koiter [41] presents a general
development of work hardening, Hill [42] presents a detailed
discussion of work hardening and its applications, and
Malvern [43] gives a concise review of the prevalent models.
The isotropic work hardening rule used here employs a von
Mises yield criterion; where the yield function is single
valued and independent of hydrostatic pressure. The yield
criterion may be stated as

$$f(\sigma_{ij}) - F(J_2) > 0; \qquad \qquad \text{(II-16)}$$

where f is the yield function and J_2 is the second invariant
of the stress deviator.

Stability in Drucker's sense leads to the statement of
normality [44] which, in turn, leads to a functional form of
the proposed constitutive model. Normality is expressed as

$$\dot{\varepsilon}^p_{ij} = \Lambda' \frac{\partial f}{\partial \sigma_{ij}}; \qquad \qquad \text{(II-17)}$$

where Λ' is a proportionality factor that depends on
J_2 and dJ_2 [45]. Once on the yield surface,
$f(\sigma_{ij}) = F(J_2)$, additional plastic deformation requires

22

$f(\sigma_{ij}) > F(J_2)$. Therefore one may write

$$\dot{\epsilon}^p_{ij} = \Lambda \frac{\partial f}{\partial \sigma_{ij}} \frac{\partial f}{\partial \sigma_{mn}} \dot{\sigma}_{mn}; \qquad (II-18)$$

where Λ is a different proportionality factor and is a function of J_2 [45]. Normality produces a linear relation between plastic strain rate and the stress rate. In order to make Equation (II-18) useful for computations, specific assumptions need to be made about the form of $F(J_2)$. Under the assumption of von Mises yielding, the yield function is the von Mises equivalent stress (σ_{eq}) and is defined as [43]

$$\sigma_{eq} = \sqrt{\tfrac{3}{2} S_{ij} S_{ij}}; \qquad (II-19)$$

where $S_{ij} = \sigma_{ij} - \delta_{ij}\sigma_{kk}$ is the stress deviator. The 3/2 factor in Equation (II-19) ensures σ_{eq} equals the yield strength when uniaxial load is applied. For a work hardening, von Mises material, an equivalent plastic strain rate can be defined;

$$\dot{\epsilon}_{eq} = \sqrt{\tfrac{2}{3} \dot{\epsilon}^p_{ij} \dot{\epsilon}^p_{ij}}, \qquad (II-20)$$

such that $dW_p = \sigma_{eq}\dot{\epsilon}_{eq}$ where dW_p is the plastic work increment [40]. The multiplication of Equation (II-18) by σ_{ij} and substitution of $dW_p = \sigma_{eq}\dot{\epsilon}_{eq}$ [40] into the result, leads to the following expression for Λ.

$$\Lambda = \frac{\sigma_{eq}\dot{\epsilon}_{eq}}{\frac{\partial f}{\partial \sigma_{mn}} \dot{\sigma}_{mn} \frac{\partial f}{\partial \sigma_{ij}}\sigma_{ij}} \qquad (II-21)$$

Then, by noting $\frac{\partial f}{\partial \sigma_{mn}} d\sigma_{mn} = dJ_2$ and $3J_2 = \sigma_{ef}^2$ the proportionality factor is simplified to

$$\Lambda = \frac{9}{4\sigma_{eq}^2 E_T} \qquad (II-22)$$

where E_T is the tangent modulus [46] of the equivalent stress-equivalent strain curve. The definitions of equivalent stress and strain are such that under uniaxial loading E_T is also the tangent modulus of the uniaxial stress-strain curve.

Finally, substituting Equation (II-22) into (II-18) leads to a specific form of the isotropic flow rule, which gives a relation between the plastic strain rate, stress deviator and the stress rate.

$$\dot{\epsilon}_{ij}^p = \frac{9}{4} \frac{S_{ij} S_{mn}}{E_t \sigma_{eq}^2} \dot{\sigma}_{mn} \qquad (II-23)$$

Elastic deformation is included by combining Equation (II-23), Hooke's law, and the total strain rate tensor ($d\epsilon_{ij}^e + d\epsilon_{ij}^p$) to yield a relation for the total strain rate

$$\dot{\epsilon}_{ij} = \frac{1}{2G}\left[\dot{\sigma}_{ij} - \left(\frac{\nu}{1-\nu}\right)\delta_{ij}\dot{\sigma}_{kk}\right] + \frac{9}{4}\frac{S_{ij} S_{mn}}{E_T \sigma_{eq}^2}\dot{\sigma}_{mn}; \quad (II-24)$$

and the stress rate

$$\dot{\sigma}_{ij} = 2G[\dot{\epsilon}_{ij} + (\frac{\nu}{1-2\nu}) \delta_{ij} \dot{\epsilon}^p_{kk}] - \frac{3G\ S_{ij}\ S_{mn}\ \dot{\epsilon}_{mn}}{\sigma^2_{eq}\ (1+E_T/3G)} ; (II-25)$$

where incompressibility ($\dot{\epsilon}_{kk}=0$) is used. By substituting Equation (II-25) into Equation (II-23) the final form of the von Mises, isotropic, work hardening constitutive model is obtained.

$$\dot{\epsilon}^p_{ij} = \frac{3\ S_{ij}\ S_{mn}\ \dot{\epsilon}_{mn}}{2\ \sigma^2_{eq}\ (1+\ E_T/3G)} \qquad (II-26)$$

II.4 Numerical Implementation of EPBEM

Simple domains, simple boundary conditions and knowledge of the loading history are all needed if exact solutions to the elastic-plastic boundary element equations (Equations II-14, II-15 and II-26) are to be found. Some exact solutions are documented [47], but seldom are researchers so fortunate.

This section will discuss an iterative solution to the elastic-plastic boundary element problems. In doing so, the surface and domain discretization, the interpolation functions used to approximate the traction rate ($\dot{t}_i$),

displacement ($\dot{u}_i$) rate, and the plastic strain rate ($\dot{\epsilon}^P_{ij}$) are presented. The system matrix formulation is discussed in detail. This discussion includes the calculation of diagonal elements, the calculation of surface stresses, and the handling of geometric discontinuities. Finally, the iterative solution scheme for the elastic-plastic problem is detailed. In order to simplify the following discussion, body forces are neglected. Also, for convenient referencing, Equations (II-14), (II-15), and (II-26) are rewritten below.

$$\dot{u}_j(p) = \int_\Gamma U^*_{ij}(s,p)\dot{t}_i(s)\,d\Gamma - \int_G T^*_{ij}(s,p)\dot{u}_i(s)\,d\Gamma +$$

$$+ \int_\Omega S^*_{jki}(s,p)\dot{\epsilon}^p_{ki}(p)\,d\Omega. \tag{II-27.A}$$

$$C_{ij}(s)\,\dot{u}_i(s) + \int_\Omega T^*_{ij}(s,\ell)\dot{u}_i(\ell)\,d\Gamma = \int_\Gamma U^*_{ij}(s,\ell)\,\dot{t}_i(\ell)\,d\Gamma$$

$$+ \int_\Gamma S^*_{jki}(s,\ell)\dot{\epsilon}^p_{ki}(\ell)\,d\Omega. \tag{II-27.B}$$

$$\dot{\epsilon}^p_{ij} = \frac{3 S_{ij}\,S_{mn}\,\dot{\epsilon}_{mn}}{2\,\sigma^2_{eq}\,(1 + E_T/3G)}. \tag{II-27.C}$$

The daily advances made in memory and speed of modern computers amaze even the most avid computer enthusiasts. However, today's computers have nowhere near the capacity to exactly model the functions and domains commonly encountered in many mechanics problems. For this reason, domain discretization and function interpolation have become a science unto themselves. Boundary element methods, just like finite element methods (FEM) and finite difference methods (FDM), need a certain amount of surface and domain quantization. Fortunately, the integral approach significantly reduces the amount of discretization necessary. As seen in Equations (II-27), both surface and domain integrals must be evaluated. But in BEM, the domain integrals are only evaluated in the plastic zone and therefore represent a significant advantage over FEM and FDM. Another important difference is that the domain discretization is used only to evaluate the domain integral. A further difference between finite element methods (finite difference) and boundary element methods lies in the solution approach. FEM and FDM approximate the solution over the domain, so the solution is highly dependent on the quantization and function interpolation. In contrast, the boundary element governing equation is solved exactly and all approximations are made in the boundary conditions.
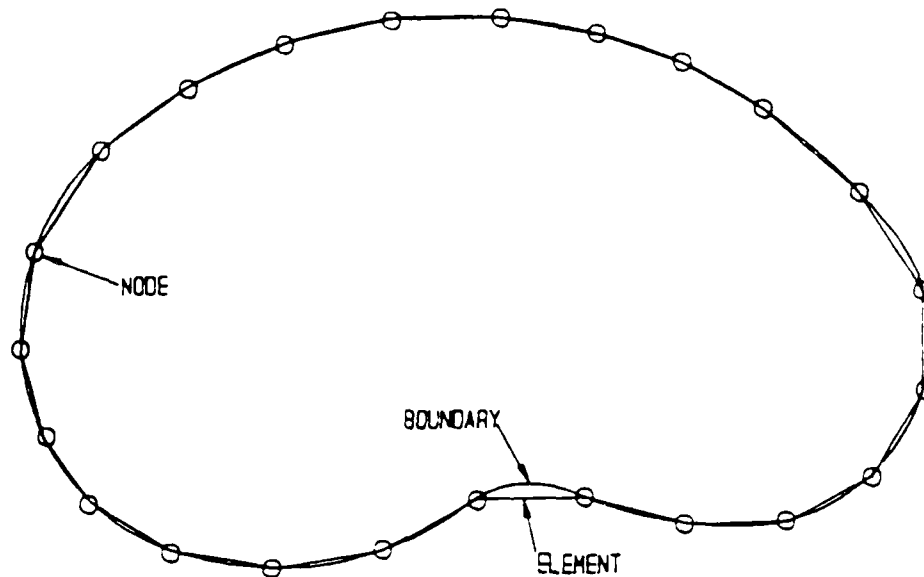
Figure 4.   Boundary modelled with straight line
            segments.

Some cases have been reported where BEM has afforded as
much as an order of magnitude improvement in accuracy
over FEM [48].

The boundary element method requires some way of
describing the bounding curve of a region; here, boundary
discretization is achieved with straight line segments
(Figure 4). Straight line segments can simply and
accurately approximate a boundary; in many cases (plates,
beams, etc.) the approximation is exact. If necessary, the
surface can be more closely modeled by increasing the number
of segments. It should be noted that there is a practical
limit to the size and number of these straight line
segments, but that limit is rarely encountered.

Now assumptions must be made about the behavior of the traction and displacements over these straight line segments. By definition, the tractions are derived from the spatial derivatives of displacement. Although consistency in derivatives is often ignored, Brebbia and Walker [49] postulated and Liu et al. [6] later showed that a consistent boundary element solution greatly exceeds
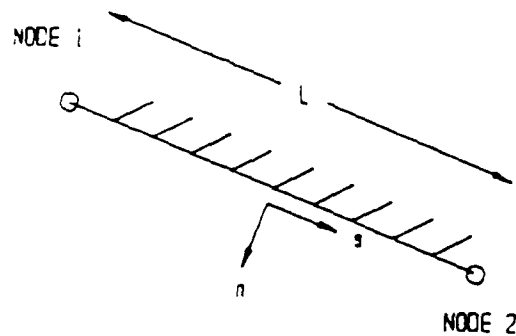
Figure 5. Representative boundary element.

comparable inconsistent routines in both computational speed and accuracy. In addition, when only displacement boundary conditions are prescribed, upwards to a 50% increase in speed can be achieved [6]. This last attribute is of particular interest in hybrid experimental-numerical methods.

The proposed EPBEM algorithm strives for a balance between simplicity and accuracy. To this purpose, the boundary displacements are assumed to vary linearly along the boundary segments. Correspondingly, the tractions are assumed constant over each segment. In BEM jargon these are

called constant (traction) and linear (displacement)
elements. Specifically, the boundary is broken up into N
elements, each element is joined to its neighboring elements
at nodes. The linear variations between nodes can be
described by (Figure 5)

$$u_i(x) = u_i^2(1+2s/L) + u_i^1(1-2s/L) \quad \text{for} \quad -L/2 < s < L/2; \quad (II\text{-}28)$$

where the superscripts 1 and 2 denote node 1 and 2
respectively, and the subscript i is 1 for x-displacement
and 2 for y-displacement. The form of Equation (II-28)
dictates that the displacement information is located at the
nodes, whereas the constant element traction information is
located at the mid points of each segment. As an aside,
more sophisticated discretization schemes are available
[13,54].

The plastic strain rate still must be quantized
before the numerical procedure can be described. The
plastic zone is discretized much like FEM. Triangular cells
are chosen with the plastic strains assumed to be constant
over each cell. This may seem identical to FEM but in
contrast to FEM, the cells are used only to evaluate the
domain integral. If the interpolating functions are given,
then the constraint equation (II-27.B) and interior
displacement equation (II-27.A) can be rewritten as

$$\dot{u}_j(p) = \sum_{m=1}^{N} \dot{t}_i(s) \int U^*_{ij}(s,p)\,d\Gamma_m - \sum_{m=1}^{N} \int T^*_{ij}(s,p)\dot{u}_i(s)\,d\Gamma_m +$$

$$\text{(II-29.A)}$$

$$\sum_{q=1}^{d} \dot{\epsilon}^p_{ki} \int S^*_{jki}(s,p)\,d\Omega_q$$

$$C_{ij}\dot{u}_j(s) + \sum_{m=1}^{N} \int T^*_{ij}(s,\ell)\dot{u}_i(\ell)\,d\Gamma_m = \sum_{m=1}^{N} \dot{t}_i \int U^*_{ij}(s,\ell)\,d\Gamma_m +$$

$$\sum_{q=1}^{d} \dot{\epsilon}^p_{ki} \int S^*_{jki}\,d\Omega_q$$

$$\text{(II-29.B)}$$

Equation (II-29.A) represents a system of 2N equations
for 2N unknowns. Its implementation is best described
through Figure 6. Each set of two rows produced by Equation
(II-29.B) is a result of placing the source point (x_s, y_s)
at the center of an element and then integrating its
influence around the surface. The source point is then
moved from element to element until the circuit is complete.
Two rows are produced because Equation (II-29.B) represents
both x and y directions. The above procedure leads to a
system of equations in the form of

$$[T]\{\dot{u}\} = [U]\{\dot{t}\} + [S]\{\dot{\epsilon}^p\}; \qquad \text{(II-30)}$$
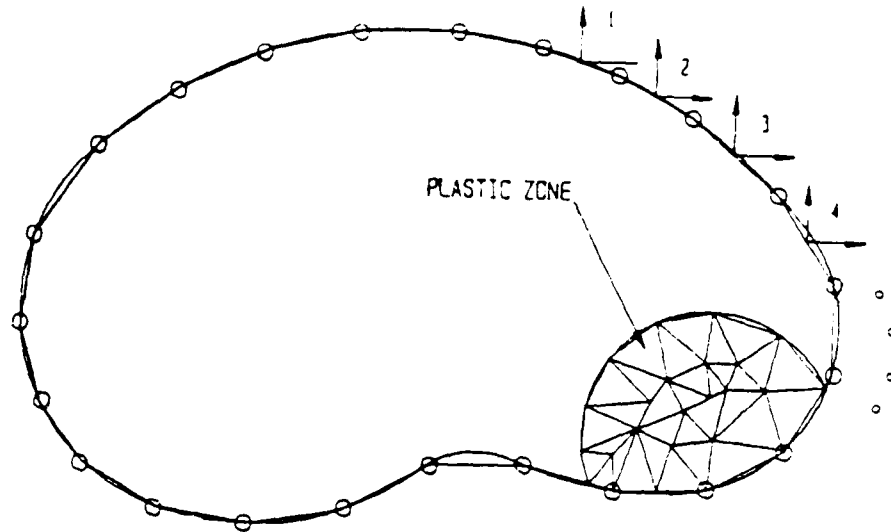
Figure 6.   Depiction of BEM solution methodology.

where [T] is the displacement coefficient matrix, [U] is the traction coefficient matrix, $\{\dot{u}\}$ are the boundary displacement rates (some of which are known), and $\{\dot{t}\}$ are the boundary traction rates (some of which are also known). The plastic strain coefficient matrix is [S], and $\{\dot{\epsilon}^p\}$ contains the plastic strain rates (all of which are unknown). Grouping the known boundary conditions and plastic strain rate information on the right hand side reduces Equation (II-30) to

$$[A]\{v\}=\{q\}+[S]\{\dot{\epsilon}_p\};\qquad\qquad\qquad(II\text{-}31)$$

where [A] is the system matrix, {v} contains the unknown
boundary conditions, and {q} contains the known boundary
conditions multiplied by the appropriate coefficients. As
will be discussed later, System (II-31) can now be solved
for the unknown boundary conditions.

There is little difficulty in using a Gaussian
numerical quadrature [50] to evaluate most of the line
integrals. However, care must be exercised when evaluating
the elements containing the singularity (diagonal elements),
as well as evaluating the domain integrals. The diagonal
elements exist but are singular; therefore, either
analytical or special numerical techniques are necessary.
The domain integral takes special care since there is a
certain amount of controversy over the derivative of
Equation (II-29.B).

The first alternative in evaluating the singular
diagonal elements is to surround the singular point with
many small sub-elements and then integrate numerically [51].
The second, and preferred, method is to integrate
analytically along each singular segment [17,35]. In any
case, the principal value coefficient matrix (C_{ij}) is
calculated analytically [17] (shown below) and added to the
diagonal terms to form the system matrix.

$$C_{11} = 1 - \frac{\alpha}{2\pi} - \frac{\cos(2\gamma)\sin(\alpha)}{4\pi(1-\nu)}$$

$$C_{12} = C_{21} = \frac{\sin(2\gamma)\sin(\alpha)}{4\pi(1-\nu)} \qquad \text{(II-36)}$$

$$C_{22} = 1 - \frac{\alpha}{2\pi} - \frac{\cos(2\gamma)\sin(\alpha)}{4\pi(1-\nu)}$$

Figure 7 shows that α is the corner angle and γ is the angle between the bisector of α and the x-axis.
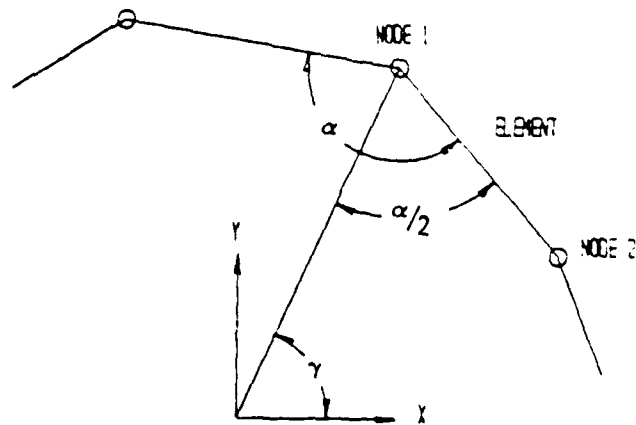
Figure 7. Enlargement of a corner used to calculate C_{ij}.

The domain integration scheme used in this algorithm is chosen to avoid the current controversy over the correct expression for the spatial derivative of Equation (II-27.A). This derivative is a dominating aspect since it defines the strain within the body. The ongoing debate revolves around the existence and the proper definition of the derivative of the plastic strain rate integral. Although well documented by Telles [18] in his introductory chapter, the salient features of the controversy are presented.

The strain at any point in the domain is defined by $2\dot{\epsilon}_{ij} = (\dot{u}_{i,j} + \dot{u}_{j,i})$. Many early researchers failed to recognize that the integration path around the domain singularity changes with the load; this path change prevents pulling the derivative directly under the plastic strain rate integral [52-55]. Bui [56] was the first to recognize this error and formulated the correct derivative; Telles and Brebbia [57] expanded Bui's ideas and then later carried them out [21]. The above techniques are both elegant and independent of the plastic strain rate shape function but they are sometimes difficult to use. Specifically, high aspect ratio cells cause the integration scheme to give erroneous results. Since the EPBEM algorithm presented here is of the constant cell type, the general approach championed by Telles and co-workers will be foregone in lieu of an implementationally easier technique.
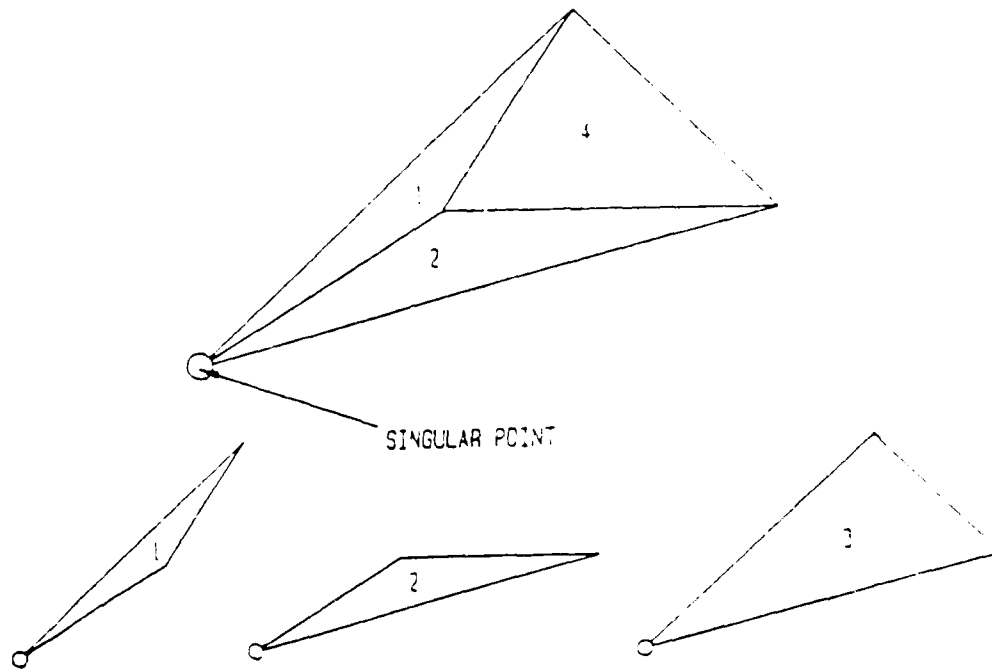
Figure 8.   Sch…e used in domain integration.

The assumption that plastic strain rate is constant over each interior cell is not only computationally simple, it also makes the above discussion inconsequential.   The constant cell approximation enables direct evaluation of the plastic strain rate integral [17,36,37] by subdividing the cell (Figure 8). The integrals over triangle 1 and triangle 2 are algebraically added to the integral over triangle 3 to give the desired integral over the cell (triangle 4).

The unit directions are defined so that the algebraic signs
are correct. Since the plastic strain rate kernal is
singular at the base point, a small region surrounding this
point is excluded in the kernal evaluation (Appendix). This
integration scheme is equally valid when the source point
coincides with the load point (Figure 9). No great
difficulty exists in evaluating the integrals; and the
question surrounding the existence of the derivatives is
moot since plastic strain rates are found via direct
differentiation.
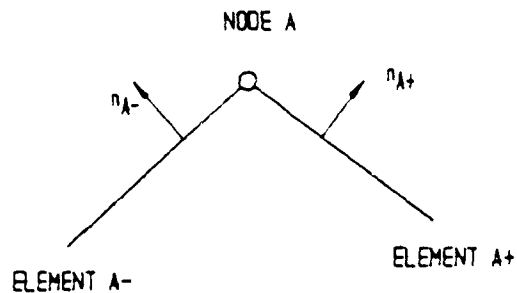
Figure 9. Singularity inside the integration
cell.

Another point of computational interest is the
evaluation of stress rates along the boundary. Since S_{jki}
has a singularity $O(r^{-2})$, the integral approach to calculate
stress rates near the boundary introduces large errors
(since $r<<1$ near the boundary). Instead, the EPBEM employs

the technique sketched by Hartmann [58]. Although
introduced in the context of elastostatics, the method is
equally valid for elasto-plasticity. There are seven
unknown quantities on any smooth boundary point in a two-
dimensional body, three stress rates $\dot{\sigma}_{ij}$ and four
derivatives $u_{i,j}$. There are also seven equations available:

1) Hooke's Law

$$\dot{\sigma}_{ij} = 2G\dot{\epsilon}_{ij} + \frac{2G\nu}{1-2\nu}\delta_{ij}\,\dot{\epsilon}_{kk} \qquad \text{(II-37.A)}$$

2) The definition of traction rate

$$\dot{t}_{ij} = \dot{\sigma}_{ij}\,n_j \qquad \text{(II-37.B)}$$

3) The derivative of $\dot{u}_i$ along the arclength.

$$\frac{d\dot{u}_i}{ds_\ell} = \dot{u}_i,x_j\,\frac{dx_j}{ds_\ell} \qquad \text{(II-37.C)}$$

Note that Equation (II-37.A) uses only the elastic portion
of the strain rates so as to keep the number of unknowns at
seven; Equation (II-37.C) uses only the elastic
displacements. Since displacements are approximated by
linear functions, the derivatives along the arc length
(Equation (II-37.C) are found directly. When constant
elements approximate displacements, finite difference

methods are typically used to provide the arclength
derivatives [59]. The seven equations assembled in matrix
form appear as

$$
\begin{bmatrix}
1 & 0 & 0 & a & 0 & 0 & -\lambda \\
n_1 & 0 & n_2 & 0 & 0 & 0 & 0 \\
0 & n_2 & n_1 & 0 & 0 & 0 & 0 \\
0 & 1 & 0 & -\lambda & 0 & 0 & a \\
0 & 0 & 0 & -n_2 & 0 & n_1 & 0 \\
0 & 0 & 1 & 0 & -G & -G & 0 \\
0 & 0 & 0 & 0 & -n_2 & 0 & n_1
\end{bmatrix}
\begin{bmatrix}
\dot{\sigma}_{11} \\
\dot{\sigma}_{22} \\
\dot{\sigma}_{11} \\
\dot{u}^e_{1,1} \\
\dot{u}^e_{2,1} \\
\dot{u}^e_{1,2} \\
\dot{u}^e_{2,2}
\end{bmatrix}
=
\begin{bmatrix}
0 \\
\dot{t}_1 \\
\dot{t}_2 \\
0 \\
\dot{u}^e_{1,s} \\
0 \\
\dot{u}^e_{2,s}
\end{bmatrix}
\qquad (II\text{-}38)
$$

where the traction rates and the elastic tangential
displacement rate derivatives are a product of the boundary
element constraint equation, $\lambda = 2G\nu/(1-2\nu)$, $a = -\lambda-2\nu$, n_i
are the normals and G is the shear modulus. The equations
for stress rates are calculated with Cramer's rule and
listed below:

$$
\dot{\sigma}_{11} = \frac{\dot{t}_1 A + G\,B_1 B_2 + G n_2^2\, C_1 C_2}{D} \quad ; \quad (II\text{-}39.A)
$$

$$
\dot{\sigma}_{22} = \frac{-G B_2 E + n_1^2\, C_1(\dot{t}_2 n_2 - G\,C_2)}{D} ; \qquad (II\text{-}39.B)
$$

$$
\dot{\sigma}_{12} = G n_1 \left(\frac{\dot{t}_1\, E + n_2 C_1 C_2 + \dot{t}_1 B_1}{D} \right); \quad (II\text{-}39.C)
$$

where

$$A = \lambda^2 n_2^2 + n_1 - a^2 n_1 n_2^2,$$

$$B_1 = a n_1^2 + \lambda n_2^2, \qquad B_2 = n_1 \dot{t}_1 - n_2 \dot{t}_2,$$

$$C_1 = \lambda^2 - a^2, \qquad C_2 = \dot{u}_{2,s} n_1 - \dot{u}_{1,s} n_2,$$

$$D = G a n_1^4 + (2 G \lambda - a^2 - \lambda^2) n_1^2 n_2^2 + G a n_2^4,$$

$$E = \lambda n_1^2 + a n_2^2.$$

With the preliminary numerical eccentricities taken
care of, it is now time to present the final part of the
iterative EPBEM solution puzzle. First the boundary
integral equation for the total strain rate is needed. By
substituting Equation (II-27.A) into strain-displacement
equation, the total strain rate looks generically like

$$\dot{u}_{i,k} = \dot{t}_j(s) \int U^*_{ij,k}(s,p)\, d\Gamma - \int \dot{u}_j(s) T^*_{ij,k}(s,p)\, d\Gamma$$

$$\hspace{6cm} \text{(II-40)}$$

$$+ \dot{\varepsilon}P_{jm} \frac{\partial}{\partial x_k} \int S^*_{ijm}(s,p)\, d\Omega$$

where

$$U_{ij,k}^* = -\frac{1}{8\pi G(1-\nu)r} (\delta_{ij}(3-4\nu)r_{,k} - \delta_{jk}r_{,i} + 2r_{,i}r_{,j}r_{,k})$$

$$T_{ij,k}^* = -\frac{1}{4\pi(1-\nu)r^2} (2[(2\nu-1)\delta_{ij}r_{,k} + \delta_{jk}r_{,i}$$

$$- 4r_{,i}r_{,j}r_{,k}](\frac{\partial r}{n}) + (1-2\nu)[n_k\delta_{ij}$$

$$+ n_i\delta_{jk} - 2n_i r_{,j}r_{,k} + 2n_j r_{,i}r_{,k}] + 2n_k r_{,i}r_{,j}),$$

and $\frac{\partial}{\partial x_k} \int S_{ijm}^* (s,p)d\Omega$ is given in the Appendix.

As previously mentioned, the singular nature of $S_{jki}(s,p)$ prevents bringing the derivative directly under the integral; therefore $S_{jki}(s,p)$ is analytically integrated and then differentiated (Appendix).

The iterative elasto-plastic boundary element solution technique is similar to the successive approximation scheme used by Roberts and Mendelson for stress function solutions [60]. The iterative approach used here is less cumbersome since the total strain rates are found directly. The instructions below list the steps in the EPBEM solution technique and Figure 10 provides a flow chart for quick referencing.

1) Apply an elastic load to bring the most highly stressed cell to a stress state near yield.

2) Find the total elastic stress and strain at each cell. For each cell, use the elastic strain as the initial guess for accumulated ϵ_{ij}^P and use elastic stress as the initial guess for the current total stress.

3) Apply a load increment large enough to cause incipient yielding. Use the load increment and the initial guess for the plastic strain rate in the following form of Equation (II-31) to find the unknown boundary conditions.

$$[A]\{v\} = \{q\} + \delta\{q\} + [\Delta\Sigma]\{\dot{\epsilon}_p\}$$

$\delta\{q\}$ = load increment

4) Use $\{v\}$ from step (3) to find the total strain rates at each cell with Equation (II-40).

5) Calculate the elastic strain rate at each cell with $\dot{\epsilon}_{ij}^e = \dot{\epsilon}_{ij} - \dot{\epsilon}_{ij}^P$.

6) Use Hooke's Law (II-12) to calculate the stress rate at each cell.

7) Add the stress increment to the current total stress in each cell and use it to find the corresponding tangent modulus (E_t) from the uniaxial stress strain curve.

8) Check each cell to see if it is beyond yield;

$$\sigma_{ef} >? \ Y;$$

where σ_{ef} is the von Mises equivalent stress (also the yield function) and Y is the current uniaxial yield strength for the cell.

9Y) If the cell has yielded; then calculate the new plastic strain rate of the cell with the isotropic work hardening, von Mises flow rule (II-33.C). Use the new total stress, E_t from step (7) and the current plastic strain rate in Equation (II-33.C).

9N) If the cell is still elastic, set $\dot{\epsilon}P_{ij}$ equal to zero.

10) Check for $\dot{\epsilon}P_{ij}$ convergence against the previous value.

11N) If the tolerance is not met, subtract the stress rate found in step (6) from the current total stress found in step (7). Then go to step (5) and start again.

11Y) If the error tolerance is met, approximate the new uniaxial yield stress for each yielded cell by the current von Mises equivalent stress.

12) If the problem is done, quit. If the problem is not finished go to step (3) and start a new increment cycle.

With possible exception of step (11N), the instructions listed above are self-explanatory. For step (11N), the current guess for the stress rate must be subtracted from the known previous total stress after each pass through an unsuccessful iteration. It is improper to add each current guess for the stress rate to the last increments total stress plus the last iterations stress rate guess. The current total stress would then be the sum of the previous total stress and all the stress rate guesses.

The above iterative solution to elasto-plastic boundary element problems is reasonably efficient and has acceptable accuracy. The technique is sufficiently general so that it is easily extended to other than boundary element methods.

$$\text{Guess } \{\dot{\epsilon}^p_{ij}\}$$

$$\text{B.E.M.}$$
$$\{\dot{\epsilon}_{ij}\} = \{x\} + \{b\}\{\dot{\epsilon}^p_i\}^T$$

$$\dot{\epsilon}^e_{ij} = \dot{\epsilon}_{ij} - \dot{\epsilon}^p_{ij}$$

$$\text{Hooke's Law}$$
$$\dot{\sigma}_{ij} = C_{ijk\ell}\, \dot{\epsilon}^e_{k\ell}$$

$$\text{Constitutive Model}$$
$$\dot{\epsilon}^p_{ij} = f(\sigma_{ij},\ \dot{\sigma}_{ij},\ \dot{\epsilon}_{ij})$$

$$\text{Tolerance Check}$$

no

yes
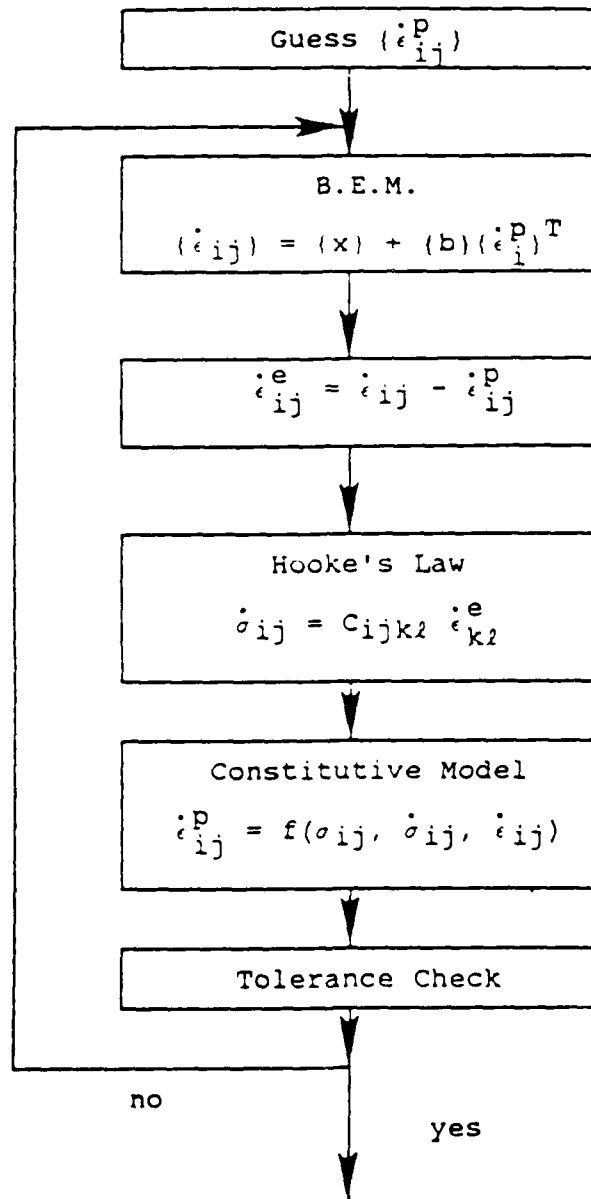
Figure 10. Flow Chart of the iterative elasto-plastic
boundary element solution technique.

When large scale yielding occurs, there is a possibility that the plastic zone will exceed the celled region. If such a case arises, one expects a reduction in EPBEM accuracy.

SECTION III

DISPLACEMENT PATTERN MATCHING

The spread of image processing applications in
photomechanics is a consequence of the availability of
equipment at affordable costs. Hardware prices continue to
decline and the power of personal computers continues to
increase. Economical mass storage, networking, graphics,
and application specific software all have increased the
proliferation of image processing in the photomechanics
field [61]. For the most part, image processing techniques
in photomechanics are grouped into two categories, fringe
analysis [62-65] and correlation techniques [6,66-68]. A
third category, pattern mapping [23,69], is emerging as
alternative with many attractive qualities. Pattern mapping
is a non-destructive technique measuring displacement and
strain and is based on image processing and syntactic
pattern recognition. It is a process by which "black" spots
on a "white" background are followed in a double exposure
type scheme. This technique offers

1)   Full field measurement.

2)   Sub-pixel registration.

3)   Greatly reduced CPU time.

4)   A highly automated technique.

5)   Relative ease of specimen preparation.

Pattern mapping was originally developed as a general purpose strain measurement technique capable of discerning large rigid body rotation and translations.   It also included a variety of strain definitions.   Fail [23] suggested that reductions in run time were achievable by tailoring the pattern mapping to a specific class of problems.   Displacement pattern matching (DPM) is a result of this suggestion.   The displacement pattern matching algorithm is developed by assuming that the experimenter can prevent appreciable rigid body motion and that displacements are the only information of interest.   As a result, a highly automated, very fast displacement tracking scheme emerged.

The DPM algorithm can be broken into three blocks: image segmentation, feature extraction, and matching. These three terms are common pattern recognition jargon but may be new to the experimental mechanics community.   To clarify the transition into the new terminology, formal definitions of image segmentation, feature extraction, matching and a fourth term, registration, are provided.

Image Segmentation is the separation of the image
into different regions, each having specific and
related properties. It is the first step in all
pattern recognition schemes and attempts to
describe or classify the image [70,71]. An
example might be to describe a landscape; that is,
segmentation of a satellite photograph, where
classification might entail distinguishing rivers
from the background [72].

Feature Extraction is the quantification of
certain characteristics of an image which are
usable in further image information classification
[73]. This process discerns important foreground
features from the background. Examples might be
lengths, areas, edges or curves [74].

Matching refers to a class of operations of
comparing to two or more images [75]. Matching is
typically used in time-varying imagery, where
motion detection is simply a matter of detecting
differences in successive images [76,77].

Registration is the comparison of two images of a
scene taken from different perspectives.
Registration is used as a measure of resolution
attainable with matching algorithms [78].

Capturing a digital image and the equipment required to do

so are briefly discussed in the next section. The ensuing

sections describe the segmentation, feature extraction, and

matching blocks of the DPM algorithm. The final section

verifies DPM through rigid body motion tests and will

attempt to assess the important characteristics that control

accuracy.

III.1 Images and Digitizing Equipment

The human eye scans the analog intensity distribution which is created by light reflecting from a scene and sends this information to the brain to be interpreted. Upon receiving the signal, the brain processes the scene and classifies the image. Ideally, computer vision should be capable of emulating this process. A quantization of the intensity distribution is necessary if a computer is to have any hope of mimicking the recognition processes of the human brain. The most primitive medium of communication for a computer is numbers (digits). Therefore, it is logical that an efficient quantization technique would be able to convert the analog intensity distribution to a digital approximation, hence the term digitize.

A digital image is a numerical approximation of a real scene, with local intensity distributions approximated by gray levels [79]. Gray levels are integers ranging from zero to an upper limit set by the hardware. The eight bit digitizing board used in these experiments affords 0-255 gray levels. These gray levels represent the darkness and are ordered to form a matrix representation of the image.

An example of the imaging procedure is given in Figure 11 where a black spot and its digital representation are provided. Key traits to note include: black appears as lower gray levels than white, the two pixel (picture element) fuzzy transition region between black and white [80], and the noise in the image. When looking at scenes containing high contrast sub-regions, the human eye has little difficulty locating boundaries between light and dark. For computer vision hardware, this process is not so simple. One would expect sharp contrast borders in the scene to be represented by a jump in gray level, when in fact, the imaging system sees a finite transition between light and dark. This fuzzy transition is a product of hardware limitations in the camera and in the digitizing board. The camera sensing array is divided into a finite number of sensing cells. Cell crosstalk, frequency limitation characteristics, and cell overlap are typical contributions of the camera to fuzzy regions [81-82]. In addition, the mismatch between the camera array size and the digitizing hardware array size increases the fuzziness. In general these array sizes differ considerably. A typical example would be four digitizing pixels representing three camera pixels, i.e. a smearing effect. Although the mismatch is not usually this dramatic, its effect is noticeable.
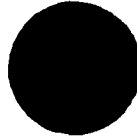
```
158 157 157 157 157 157 157 155 155 156 157 158 157 155 156 158
158 157 157 158 156 156 156 154 155 155 155 156 157 156 156 157
156 156 157 156 155 156 155 153 155 157 157 157 157 158 158 158
155 154 154 156 154 151 151 150 149 152 155 156 157 156 156 157
157 157 157 157 155 150 140 129 130 137 148 155 157 156 158 158
155 155 157 155 147 134 107 74  68  97  133 148 152 156 158 156
157 156 156 153 139 103 62  54  62  67  94  136 154 156 158 158
155 156 156 146 118 72  52  56  54  49  58  95  142 158 156 157
155 156 154 137 93  54  52  55  52  56  63  85  133 159 154 156
156 156 152 130 87  50  48  54  49  49  60  75  117 155 158 156
157 156 148 120 72  54  55  53  52  53  57  64  99  145 158 155
155 153 146 114 66  51  55  49  47  51  54  56  85  140 159 154
158 155 143 111 63  50  51  47  50  53  53  60  95  146 159 154
157 154 142 106 58  49  55  47  46  54  56  59  88  137 158 155
155 154 146 109 59  51  57  53  54  56  55  59  89  140 158 154
156 154 146 114 66  50  53  52  52  53  54  56  90  144 158 153
158 157 150 124 73  48  52  52  50  52  54  65  107 149 155 155
157 154 152 132 88  54  55  56  51  51  53  71  117 154 157 156
157 155 155 144 106 56  50  60  53  54  62  84  129 157 156 156
158 158 156 151 130 84  53  56  59  57  69  105 146 157 154 155
159 158 157 156 149 119 69  50  60  68  93  135 156 156 158 158
157 158 158 156 154 143 116 83  80  103 133 152 155 155 156 157
158 158 159 157 156 155 149 142 140 143 150 156 158 157 158 159
158 159 157 157 157 154 152 152 151 151 152 155 158 158 157 157
158 157 156 158 158 156 157 156 154 155 158 159 157 155 156 158
156 156 157 158 158 158 157 158 157 156 158 157 155 157 157 158
```

Threshold=121

Figure 11. A black spot and its digital representation.

In Figure 11 the spot is uniformly black; unfortunately noise degradation prevents the image from reflecting the uniformity. Degradation is apparent in the fluctuating gray level representation of black in the spot and results from optical or electronic sources. Spherical aberration, coma, astigmatism, non-uniform illumination, and dust are just a few examples of optical noise [83]. Electronic noise may come from thermal effects in the imaging array, the digitizing process, electro-magnetic interference, or may just be inherent to the imaging array [80-82]. Regardless of the source, DPM regards noise as random and therefore having a zero mean distribution.

Now that some of the ideas and important aspects of a digital images have been illustrated, the equipment and procedure for obtaining a digital image can be described. Figure 12 depicts a typical personal computer based digitizing system. The imaging device used here is a Sony XC-38 CCD camera, a Datacube IVG128 Video Acquisition and Display Board (384H x 512V) which quantizes the image with its digital form displayed on a PVM-1271Q/1371QM Sony studio monitor. All image processing is done on a PC's Limited 286-8 Personal computer equipped with a math co-processor and EGA graphics.

PERSONAL COMPUTER
WITH A DIGITIZING
BOARD

VIDEO MONITOR

CCD CAMERA
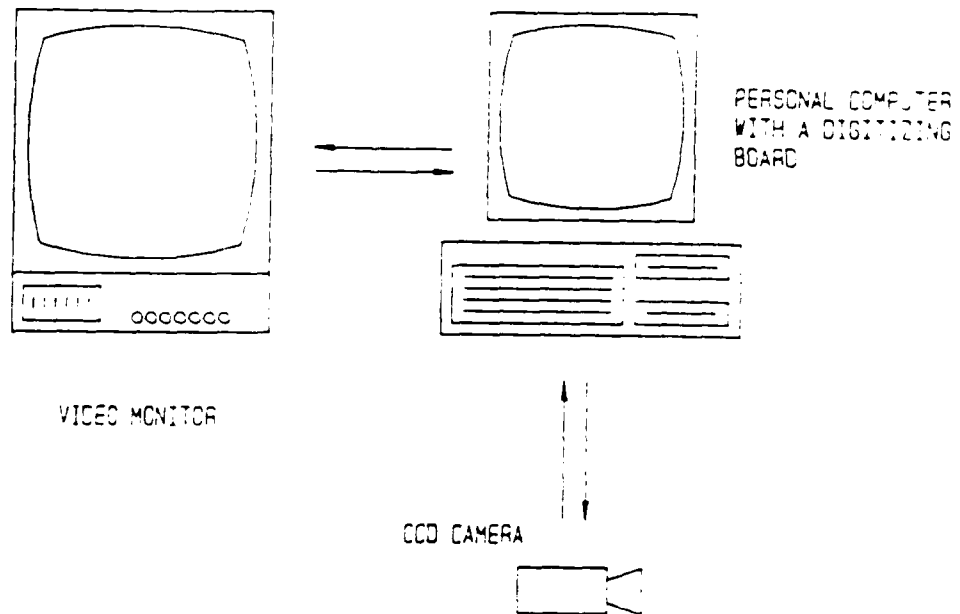
Figure 12.   Typical personal computer based digitizing
system.

Digitizing is software controlled. On command, the

frame buffer stores the image as a matrix of signed bytes

representing the gray levels. This two-dimensional matrix

is also available to the user on software control. On

software control, the analog signal from the CCD (charge

couple device) camera is quantized with an analog-to-digital

converter and then mapped to the appropriated gray levels

by a software selectable look-up table. The image size

stored in the frame buffer is 384H x 485V to conform with

the RS-170A, 60Hz United States interlaced video standard.

The 384H x 512V image conforms to the CCIR, 50Hz. European

interlaced video standard. The frame buffer is accessible
to the CPU (central processing unit) through the personal
computers I/O page [84]. VNA Systems Incorporated's Digital
Correlation Metrology software package provides software
control of the digitizing process.

III. 2 Segmentation

A decided advantage of displacement pattern matching is
the limited prior knowledge required for success. Success
of the technique hinges on the placement of high contrast
spots (dark spots on a light background) at locations where
displacement is desired. Implicit in this knowledge is the
idea that the images are binary, that is, the gray levels
should be either black or white [85]. In keeping with the
automated methodology, DPM does not need prior knowledge
about the number of spots, spot area or any other
distinguishing feature. The primary function of
segmentation is to locate the important regions of an image.
Since DPM images are binary, segmentation consists of
identifying those individual regions defined as black (the
spots) since they contain the desired information [86].

Segmentation typically (as is done here) starts with
some form of characteristic feature thresholding [87]. In
essence, a value of some characteristic feature of the image

is chosen as a basis on which to make decisions. This pivotal value is known as the "threshold". In DPM, the characteristic feature is the gray level and the threshold is the parameter used to discriminate between black and white. All gray levels above the threshold are white and all gray levels below are black. The transformation to a true binary gray scale enables a border following scheme to locate the spots. Discerning if each spot is a true spot or if it should be discarded is segmentation's culminating decision.

Once the threshold is chosen, raster scanning starts. A raster scan is nothing more than a row by row or column by column evaluation of each pixel for some prescribed property; in this case to find the first spot (gray level < I_T). When DPM locates a black pixel, the gray levels of its eight nearest neighbors are checked. If at least one neighbor is black then DPM has located a spot. If none of its neighbors are black, then DPM considers the center pixel as a false spot. Once a true spot is located, a general border following scheme developed by Rosenfeld [88] and specialized to only find outside edges [89,23] 'frames' the spot. Framing the spot is the process by which a complete clockwise circuit around the border is traversed, storing only the left most, right most, highest, and lowest pixel locations (L, R, T, B respectively) for the feature extraction. To account for the transition between black and

55

white, the frame automatically expands by two pixels in all directions (Figure 11). With the first spot framed, the raster scanning continues. This process is repeated until the entire image is examined.

False spots larger than one pixel in diameter are entirely possible, especially when the scene is significantly magnified. An automated method of discerning false from true spots is therefore required. Experience indicates that the areas of false spots are much smaller than their legitimate cousins (area is defined as A = [R-L][B-T]). A spot area larger than one third the average spot area (averaged over every framed spot) is a true spot. This definition is completely arbitrary but it proved to be 99% reliable for the spot sizes used in this research.

III.3 Feature Extraction

Features are selected measurements which are either invariant or less sensitive to typical system distortions [93]; they tend to distinguish the object from its background. Two types of features are present in the DPM images, statistical and structural [90]. The statistical features are the frame boundaries: L, R, T, B, and the spot centroid. The structural features are the spots themselves. Since segmentation simultaneously extracts the frame and the spots, only the centroids need be extracted.

The spot centroids are calculated using the true gray
levels in the frame and pixel locations (i,j) in the matrix
[80]. Mathematically stated the centroids are

$$\bar{x} = \frac{\displaystyle\sum_{i=T}^{B} \sum_{j=L}^{R} j I(i,j)}{\displaystyle\sum_{i=T}^{B} \sum_{j=L}^{R} I(i,j)}$$

and

$$\bar{y} = \frac{\displaystyle\sum_{i=T}^{B} \sum_{j=L}^{R} i I(i,j)}{\displaystyle\sum_{i=T}^{B} \sum_{j=L}^{R} I(i,j)}$$

where $I(i,j)$ is the gray level at element (i,j) in the image
matrix. The influence of the zero mean noise on the
centroid calculations is presumed to average to zero.

III.4 Image Matching

Zero rigid body motion reduces the syntactic pattern
recognition language [91] of DPM from context sensitive to
context free [92]. Pattern mapping requires each spot to be
located at the same "address" before and after deformation
[23]. In computational space, this means each spot must

always be surrounded by the same neighbors. If this is not the case, that spot is out of context which means it makes no syntactic sense. DPM makes no such requirement. The spot locations are stored in the order in which they are found. Pattern matching [93] is then used to find the spots in all ensuing registered images. Ordering the spots by their correct "addresses" is no longer crucial to finding the next image's spots; therefore, the spots do not need to be in context to make syntactical sense.

An instructive approach to describing pattern matching is to take a figurative step back and simply look at the physical nature of a typical solid mechanics problem. The question is "what are the displacements at points a, b, and c?" To answer this question correctly, each spot must be examined after deformation and compared to its previous location. Successive load increments produce a sequence of comparisons. In elasticity and incremental plasticity, assuming spot motion to be small relative to spot size is restrictive but certainly reasonable. This indicates that each sequential image should closely resemble its predecessor. The above description of events is not unique; Rosenfeld and Kak [88] (pages 50-51) give an almost identical description of events but their discussion pertains to time-varying imagery.

Time-varying imagery is a popular form of pattern
matching [75]. It is a sequential registration technique
used in motion detection, object tracking, and dynamic scene
analysis; therefore, it is well suited for discerning
displacements. Here, spot motion is measured by local
matching of the segmented spots. In essence, the location
of a spot in the image is assumed near its location in the
previous sequential image. Therefore, instead of raster
scanning the entire new image, only the previous framed area
is scanned.

If the displacement field carries the spot out of the
original frame area then the search region is expanded to

$$A_n = [L-R][B-T]n^2, \quad n=2,3,4\ldots \quad \text{(III-4)}$$

where A_n is the area of the search region and n is the
number of search region expansions required to find the spot
(Figure 13). When the search region encompasses
more than one spot (Figure 14) or a wrong spot only
(Figure 15), a one-to-one match is not guaranteed and the
matching process fails. Therefore, over-expansion defines a
restriction on DPM, but at the same time somewhat relaxes
initial assumptions of the matching scheme. The spot
displacement must be smaller than or equal the distance from
the original spot to the closest spot in the current image

n = 3

SPOT IN CURRENT
IMAGE

n = 2

n = 1

SPOT IN PREVIOUS
IMAGE
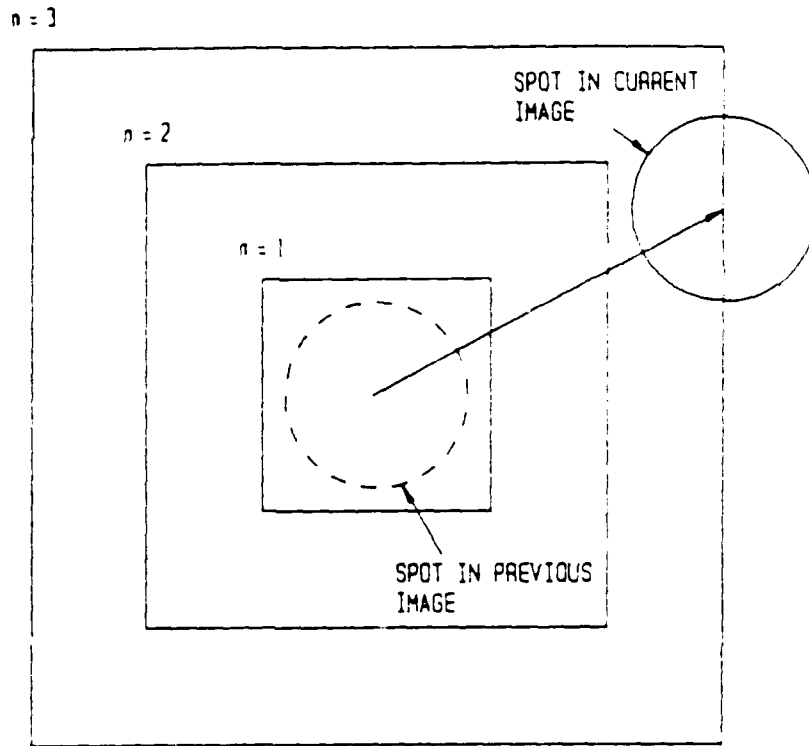
Figure 13.   Search region expansion.

(Figure 15).   This critical distance is easily gaged.   For

example, in a square array of spots, the maximum

displacement can never be greater than 0.7071 times the

smallest original spot spacing.   Spot displacements are *no*

longer restricted to being small compared with the spot

diameter.
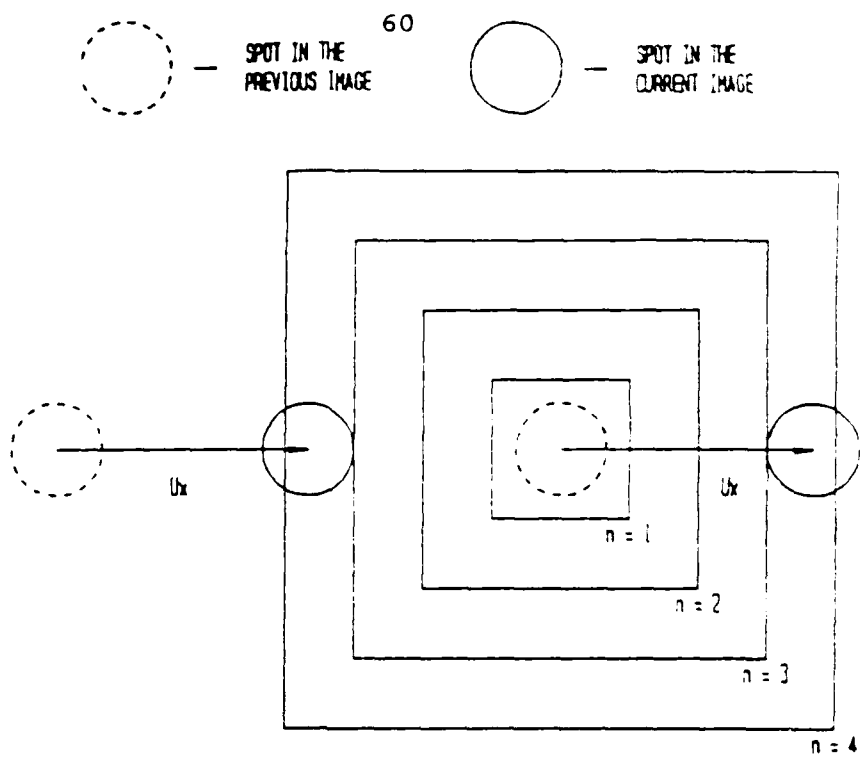
Figure 14.   Search region encompassing more than one
   spot.
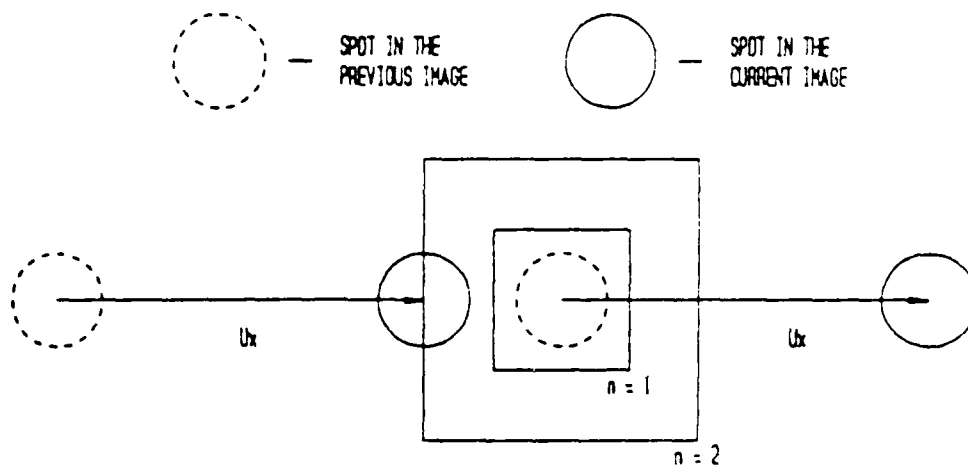
Figure 15.   Search region encompassing the wrong spot.

A special search region expansion case occurs near the image edge. When the displacement field carries a spot close to the perimeter of the image, the expansion may try to extend the search region beyond the image border, the results of which are unpredictable. The search region is therefore contoured to the image edge if the region encounters the perimeter.

With a one-to-one correspondence established between segments in successive images, statistical feature extraction can proceed. The centroid of each spot is calculated by Equations (III-2) and (III-3) and the x- and y-coordinates of the centroids in sequential images are subtracted to find the displacements

$$u_x = X_n - X_{n-1} \qquad \text{(III-5A)}$$

and

$$u_y = Y_n - Y_{n-1}. \qquad \text{(III-5B)}$$

In these displacement definitions, n refers to the current image. The units of displacement are pixels but can be converted to a units of length through calibration.

III.5 Rigid Body Motion Tests

In this closing section, the limitations of displacement pattern matching are explored. A series of rigid body motion tests, each with different spot diameters,

evaluate the accuracy of DPM. In the process, general accuracy characteristics, accuracy versus spot size, effect of image averaging on accuracy and the consequences of search region over-expansion are examined.

Each rigid body motion test consists of tracking the 5x5 array of spots shown in Figure 13 through four horizontal 0.025 (±0.001) inch increments. Spot areas are easily altered by magnification with a zoom lens.

These tests produce results that are difficult to assimilate and make system evaluation unnecessarily hard. A statistical approach reduces the information to a more understandable form. For a given magnification, the 25 spots in the array are subjected to four equal increments, yielding 100 displacement values which should be identical. Unfortunately, the displacements returned by DPM are not all equal. For the sake of comparison, the standard deviation of the 100 displacement values is calculated and normalized by the accompanying mean. This number is a measure of the amount of deviation from the applied constant displacement and serves as a vehicle to evaluate spot size.

The results in Table 1 show that there is a definite lower limit on spot size. Although difficult to say precisely, a spot diameter smaller that ten pixels is considered suspect.

Table 1. DPM error as a function of spot size.

DIAMETER (PIXELS)	STANDARD DEVIATION DIVIDED BY THE MEAN
6	0.019872
9	0.003052
1.:	0.003203
16	0.004553
18	0.004842
24	0.007174

Ideally, all spots in the array should give the same displacement (for rigid body motion). System and experimental error degrade this idealization and produce a certain amount of variance from spot to spot. The effect of system error can be seen by examining one increment of the 16 pixel diameter spots. The average displacement (over the 25 spots) is 5.183 pixels with a standard deviation of 0.0039 pixels. Averaging images from the same scene reduces the influence cf random system noise (cell crosstalk, thermal, electromagnetic, etc.). To show this, four images of each 16 pixel diameter spot scene are averaged before using DPM. The results show a significantly reduced standard deviation (0.00255 pixels) which suggests a more accurate measure cf displacement (5.181 pixels). Henceforth, all hybrid experiments use four image averages.

"False system displacement" is a result of the variance in displacement between spots in the same image and can be evaluated through self-registration. If an image is registered with itself, each spot should measure zero rigid

body motion. But instead the system displacements are returned. Table 2 reveals the displacement errors introduced by the system and represents the lower accuracy limit afforded by DPM and the hardware.

Table 2. DPM system displacement as a function of spot size.

DIAMETER (PIXELS)	MEAN SYSTEM DISPLACEMENT (PIXELS)
6	0.002251
9	0.001435
14	0.001063
16	0.001632
18	0.002117
24	0.001562

The above errors are inherent to feature extraction and are somewhat abstract; that is, no definite values can be used to discriminate good from bad. Search region over-expansion is different in this respect; over-expansion defines the limit to the displacement increment size. For horizontal rigid body motion, one expects the matching to fail when the displacement reaches one half the spot spacing. This limit is easily verifiable through a simple experiment. A 5x5 array of 0.05-inch diameter spots is again tracked through 0.025-($\pm$0.001) inch increments; but this time the increments are continued until the matching fails. The results are shown in Table 3 for a spot spacing of 0.2 inches and a spot diameter in pixels of 14. As

predicted, the matching is precise until a displacement

greater than 0.1 inch is applied. The limit on displacement

increment will not be as easily identifiable when structural

distortions are encountered, but a safe rule of thumb is not

to exceed one fifth of the smallest spot spacing.

Table 3. DPM search region over expansion.

APPLIED DISPLACEMENT (inches)	MEASURED DISPLACEMENT (inches)
0.0	0.00005
0.025	0.0249
0.05	0.0499
0.075	0.0751
0.1	0.0996
0.125	0.0286

Displacement pattern matching is an accurate, efficient

means of tra king displacements. All DPM calculations are

performed on an 80287-8 based personal computer with run

times averaging about 31 seconds per increment.

SECTION IV

HYBRID DPM-EPBEM TECHNIQUE

Both the elastic-plastic boundary element and
displacement pattern matching algorithms have been
individually verified, but the ultimate goal here is to
construct a single successful stress analysis tool by
meshing these two techniques. Accordingly, this chapter
presents a hybrid DPM-EPBEM and its experimental
verification. The following sections describe the
experimentation, specimen preparation, and verification
tests.

IV.1 Working Environment

In general, combining two programs written in the same
language is a trivial matter. But, when the two programs
are written on two different computers and use two different

D:\JIMMAP>del scratch.dat . . .

D:\JIMMAP>del cellook.dat

D:\JIMMAP>pause   To Exit Graphics Mode Type 'RESET'.
Strike a key when ready . . .

PERCENT= 10.307
THRESHOLD 118
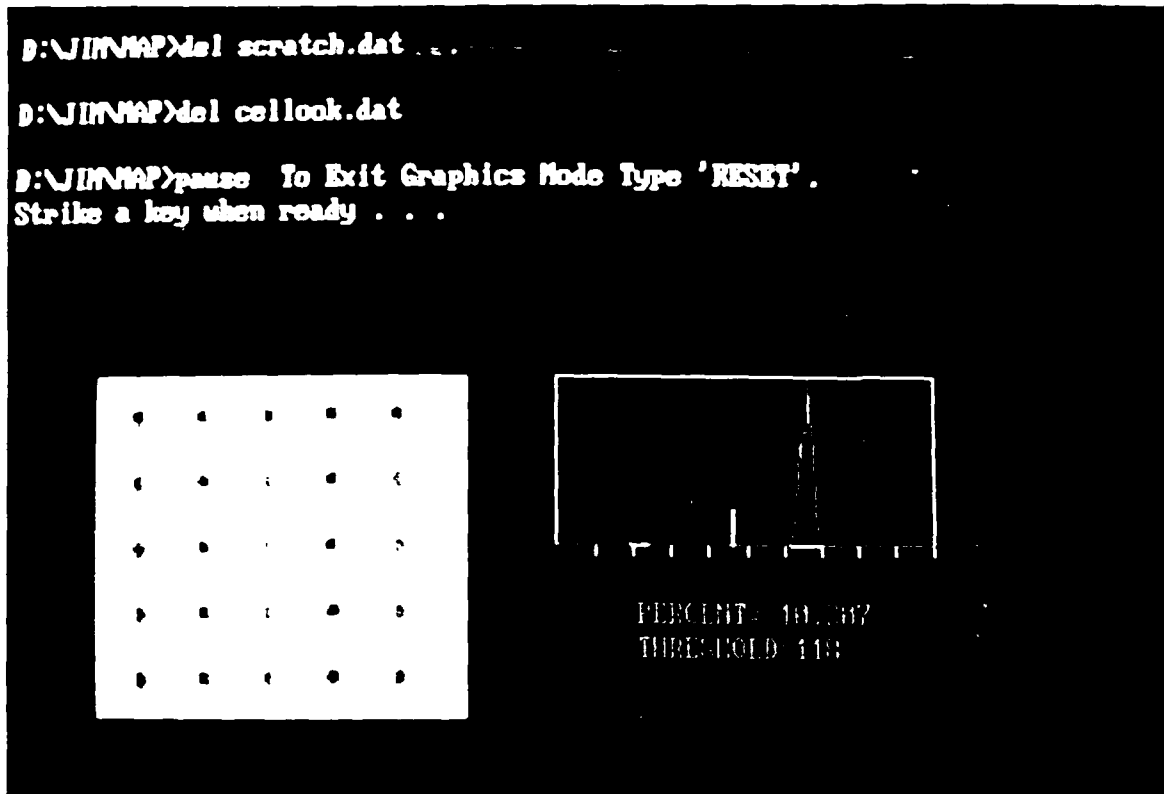
Figure 16.   Graphical Working Environment

languages the process is significantly more complicated.

Here, DPM is written on a PC's Limited 286-8 personal

computer and EPBEM is written on a Digital VAX 11/750.

These two computers have no direct means of communicating

with each other, so a third program, PROCOMM, is used as an

interpreter.   To run DPM-EPBEM, the image of each increment

is digitized and the resulting digital representation is

stored in such a way that DPM can either access these files

interactively or in batch mode. In any case, the user
controls the program through a graphical working
environment.

The working environment shown in Figure 16 provides
critical information for real time evaluation of the
program's progress. A binary pseudo-image shows the scene
currently being analyzed. Included in this picture is a
window encompassing the segmentable portion of the image.
The pseudo-image is produced by averaging each set of
sixteen nearest neighbors and then thresholding. The result
is a 94H x 121V matrix representation of a binary image.
This representation, as opposed to a 384H x 484V, is
necessitated by the limited dynamic memory afforded by
Microsoft's DOS. On the right of the pseudo-image is a
histogram of the true image with the location of the
threshold indicated by the vertical line. The corresponding
value of the threshold is given below the histogram. Also
provided below the histogram is the percentage of pixels
with the most frequent gray level. All this information
aids in evaluating the performance of the DPM.

Above the pseudo image and histogram shown in
Figure 16, is a region of the screen reserved for any
necessary software commands. That portion of the screen is
called the editor zone. After each set of displacements is
determined by DPM, the communications program, PROCOMM, is
evoked through a batch file. The batch file logs onto the

VAX, transfers the displacement files, and starts EPBEM. During this process, the editor zone displays each batch command as it is executed. Once the VAX attains control, all of the graphics are temporarily suppressed; and after EPBEM has completed the necessary calculations, the VAX maintains control. VAX control enables the user to transfer the stress and strain information back to the host computer (personal computer), to return to the host computer, or to log off. Regardless of which is chosen, all of the desired stress information is stored on the VAX and can easily be retrieved for further analysis.

IV.2 Experimental Setup and Specimen Preparation

This section provides a description of the equipment and of the general experimental setup. Since EPBEM is a two-dimensional code, only plane stress or plane strain loading conditions can be examined. All specimens are of the plane stress type and are produced from a ductile aluminum alloy (1100-H14). Loads are applied by a Material Testing System (MTS) machine. A schematic of the setup is given in Figure 17. The testing machine is manually controlled to produce either constant load or constant stroke.
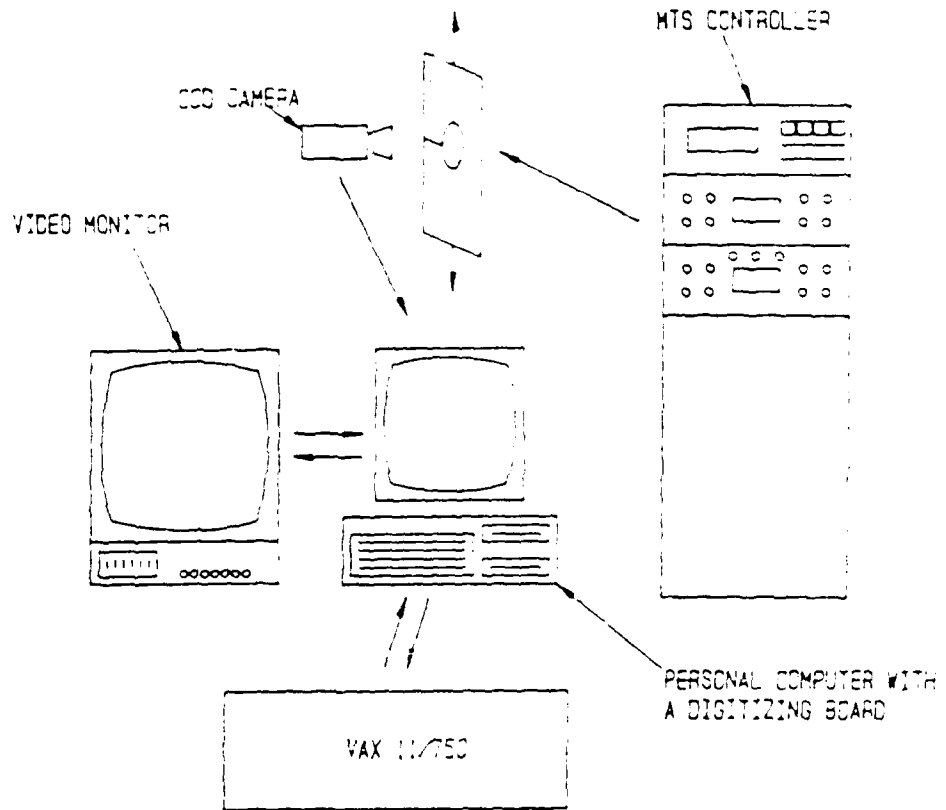
Figure 17.   Schematic of the experimental set up.

As described in Section III, DPM depends on the application of high contrast spots to the specimen. The aluminum specimens are painted flat white in order to produce the high contrast background for the black spots. Initial painting attempts resulted in the paint chipping and cracking under load. Since DPM perceives chips or cracks as spots, one must undertake means to stop this phenomenon from occurring. Each specimen is first thoroughly sand blasted to remove gross deposits of aluminum oxide. They are then cleansed in a bath of isopropyl alcohol. Following air drying, each specimen is scrubbed carefully with AMCHEM's Alumiprep 33 (stock no. DX533) to remove the remaining corrosive oxidation and to chemically etch the surface. The final treatment is a generous scrub and bath in AMCHEM's Alodine 1201 (stock no. DX503). This treatment chemically stabilizes the aluminum surface and provides a long lasting paint adhesive. An additional advantage of this procedure is that it leaves a distinctive amber stain where the coating process is successful. The specimens are then air dried and painted with flat white KRYLON enamel. The entire process, from start to finish, requires about ten minutes per specimen and provides a painted surface which does not chip or crack until near catastrophic failure loads are applied.

Spot application followed an iterative process until finding a satisfactory procedure. The primary concerns here

are uniformity in spot diameter and darkness. Best results are obtained by using typical "rub-ons" commonly found in office supply stores; the grammatical periods are far more consistent in area and darkness than any attempted painting or staining procedures. The periods are simply rubbed on at the locations where the displacement is desired.

Three plane stress experiments are presented in order of increasingly complex states of stress. The first test examined is a thin sheet under uniaxial tension, the second test is a thin rectangular sheet with a central hole, subjected to tensile end loads (perforated strip tensile test) and the final test is a thin rectangular sheet with symmetric ninety degree V-notches. The 1100-H14 aluminum used for all specimens has the following material properties: $E=10,713.$ kpsi, $\nu=.33$, and $Y_0=15,000$ psi.

EPBEM requires the uniaxial stress strain curve in the iterative solution. To accommodate EPBEM, the uniaxial true stress-engineering strain curve is found experimentally by applying known loads to a uniaxial test specimen with the MTS machine and monitoring a one-inch gage length with the MTS supplied extensometer. The stress-strain data is fitted with two piecewise continuous curves. The elastic and knee portion are fitted with the Ramberg-Osgood Law [94]; and the work hardening portion is approximated with a linear fit. The approximate and experimental stress-strain curves are given in Figure 18.
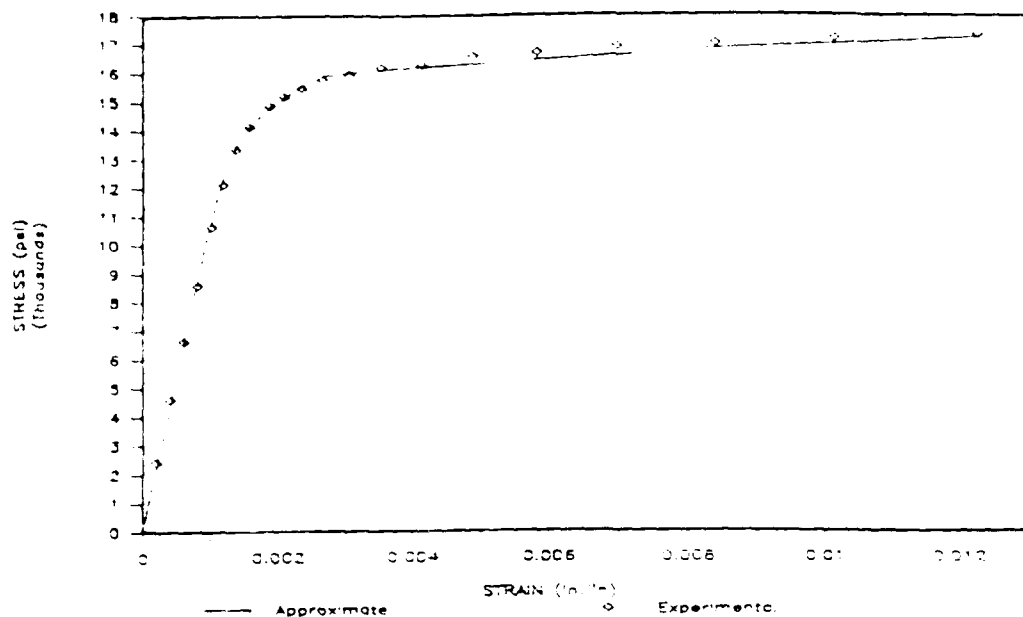
Figure 18. Uniaxial stress-strain curve for 1100-H14 aluminum.

IV.3 Calibration

Prior to each experiment, the digitizing system is calibrated carefully so that DPM results are accurately converted from pixels to units of length. The calibration constant is a function of magnification so that the first step in calibrating the system is to set the desired magnification and to keep it fixed for all load increments. Next, a 5x5 array of black dots is placed in the focal plane and given five equal vertical displacements; the array is

digitized after each step. Since all of the displacements are equal, a linear relation exists between the displacements returned by DPM (in pixels) and the measured displacements; the slope of this curve is the calibration constant. The steps to calculating the calibration constant are as follows:

1) Apply each load increment.

2) Store the four image averages of each scene.

3) Calculate the average rigid body displacement of the 25 spots in each scene.

4) Plot the average displacement (in pixels) versus the measured displacement (in units of length).

5) Use a linear least squares fit to find the slope.

The imaging array of the digitizing board used in these experiments is rectangular; therefore, the y-calibration constant differs from the x-calibration constant. To accommodate the rectangular imaging array, the above calibration procedure is repeated with horizontal displacements. A typical experiment produced x- and y-calibration constants of 369.5 and 523.3 pixels/inch, respectively. With system resolution on the order of .1 pixels, the displacement resolution is on the order of .0001 inch.

IV.4 Uniaxial Tension Test

Before describing the hybrid experiments, it should be noted that no attempt is made to relax machining induced work hardening in the specimens. Although care is taken to use sharp tools and slow cutting speeds, no annealing is performed. The specimens for all experiments are produced from the same sample of aluminum; and the uniaxial stress strain curve for each specimen is assumed to be the same.

From the least complex test of DPM-EPBEM, uniaxial tension, one expects to uncover any limitations of the hybrid technique. With this in mind, the hybrid analysis of a uniaxial tension specimen is described. The dimensions of this plane stress specimen are nine inches tall, one-inch wide and .0625 inches thick (all specimens examined have these nominal dimensions). The spots are applied to the specimen as indicated in Figure 19 and as shown in Figure 20. Two interior triangular cells are used to model the region enclosed by the spots, with DPM providing displacement boundary conditions at all but the free surface. One should note that only the region encompassed by DPM is modelled by the boundary element method and that the size and location of this region are completely arbitrary. Figure 12 shows a plot of the x-component of
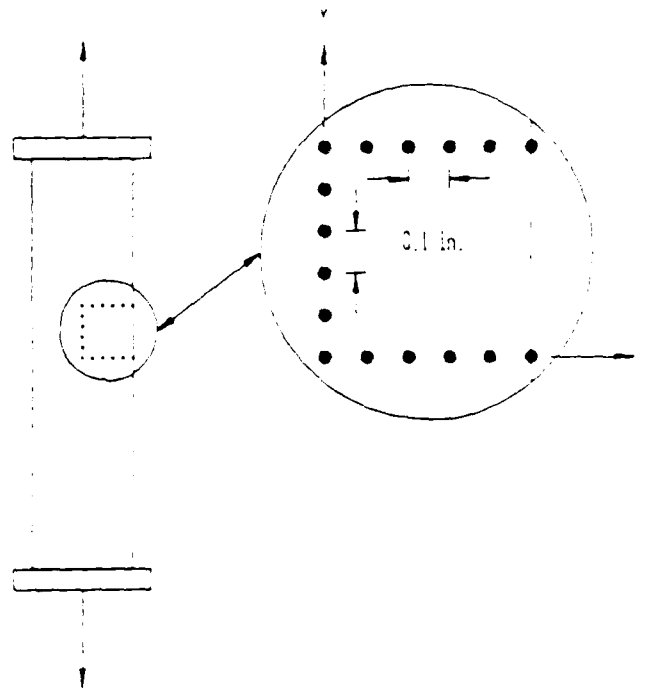
Figure 19.   Schematic of the spot locations on the
             uniaxial tension specimen.

displacement which is calculated by DPM at (x=0.25 in.,

y=0.0 in.). The results conform to the shape one expects

for a load-displacement curve of weakly work hardening

materials. A little more convincing is the plot shown in

Figure 22, which provides the stress-strain curve calculated

by DPM-EPBEM along with the experimental version. Two

interesting characteristics of note are the good correlation

between the MTS and DPM-EPBEM results and the limited useful

range of DPM-EPBEM.
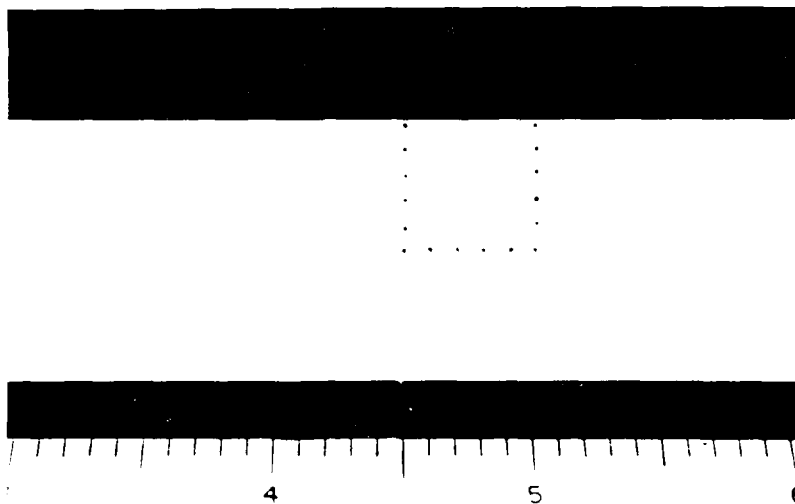
Figure 20. Photograph of the spots applied to the
uniaxial test specimen.

On the lower end, the DFM-EDSEM curve is unreliable
until approximately 4% of the proportional limit. This is
a result of the rigid body motion introduced by imperfect
alignment of the specimen in the MTS wide grips. Although
the specimens are aligned as carefully as possible, no
aligning gages are used. As the initial load steps are
applied, the specimen adjusts itself to evenly distribute
the load. The redistribution introduces both rigid body
rotation and translation. A second source of rigid body
motion comes from the specimen slipping while the wire
grips are locking down. This motion occurs during the
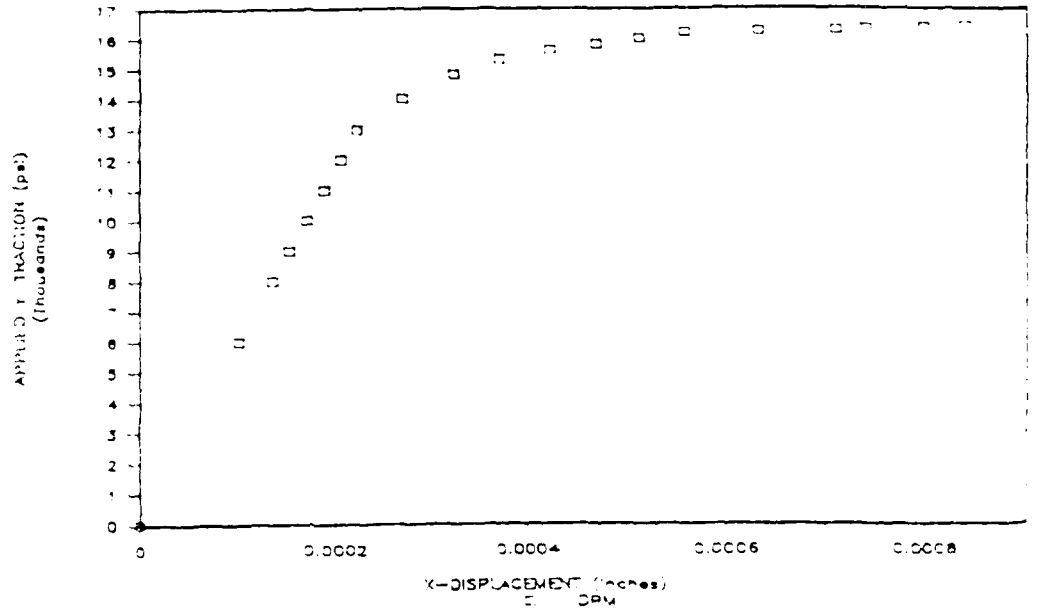
Figure 21.   Load-horizontal displacement curve for (x=0,y=.25).
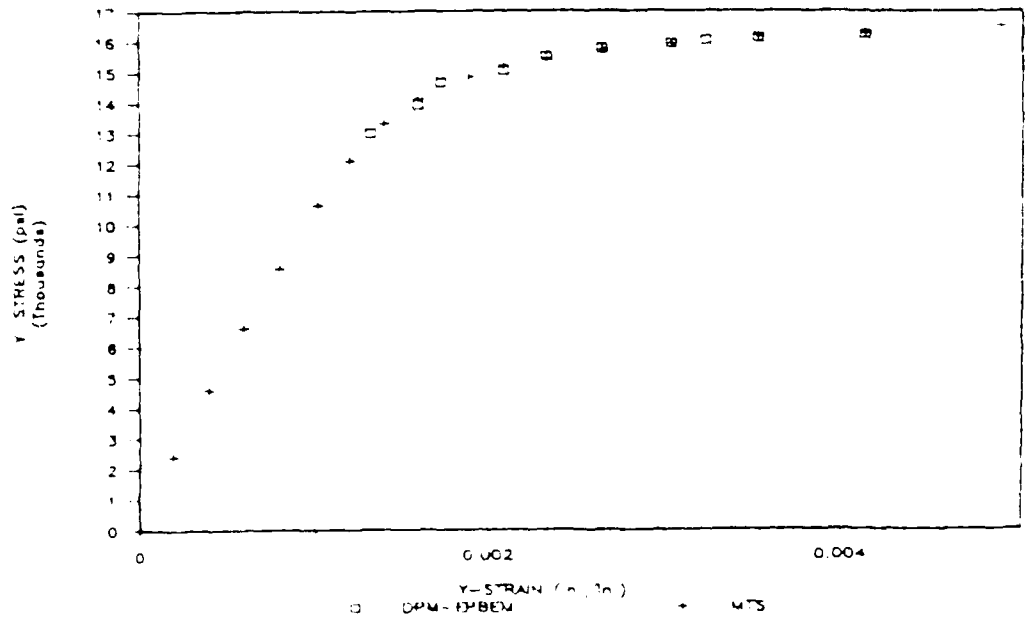
Figure 22.   Experimental and DPM-IPBEM uniaxial stress strain curve.

initial loading steps and although it is less pronounced
than the rigid body rotation from specimen misalignment,
this slippage is certainly significant.

DPM is able to discern the rigid body motion from both
sources and passes this rigid body motion information to
EPBEM. Unfortunately, EPBEM expects the constrained
displacements and has no means to separate out the rigid
body motion. Therefore, the boundary element routine
calculates erroneous stress and strain values.

Whereas DPM is responsible for the lower performance
limit, EPBEM is responsible for the upper performance limit.
EPBEM expects a work hardening material and has difficulty
converging to a solution for a perfectly plastic material.
The upper limit results from the fact that 1100-H14 aluminum
behaves in an almost perfectly plastic manner. At high a
stress, the flat portion of the stress strain curve causes
the iterative solution procedure to become unstable;
essentially, the initial strain procedure fails to converge
to a single value. It is believed that the load increments
in the flat portion of the stress-strain curve produce
strain increments too large for the initial strain solution
procedure to assimilate. An upper performance limit is
typical in all of the experiments performed but it varies
with loading conditions and geometry. Still, the DPM-EPBEM
upper performance limit usually occurs at an equivalent
stress of 16,500 psi. Overall, the uniaxial tension test

exhibits dependable results within a specific equivalent stress range and, as anticipated, unmasks basic weaknesses of the DPM-EPBEM hybrid technique.

IV.5 Perforated Strip Tensile Test

The uniaxial tensile test produces comforting results. In addition, the results establish both the accuracy and the performance range of the hybrid technique. This next test seeks the solution to a more realistic engineering problem and, among other important details, the perforated strip exposes DPM-EPBEM to a stress state containing high stress gradients. The stresses calculated by the hybrid technique are compared to both ANSYS finite element and Theocaris and Marketos' experimental results [95].

The spots are applied to the specimen at the locations specified in Figure 23 and shown in Figure 24, where the domain enclosed by the spots is modelled as seen in Figure 25. A careful comparison between Figure 25 and Figure 23 reveals that not all of the DPM spots and EPBEM nodes are found at the same locations. The finite size of the spots establishes a practical limit to the spot spacing; therefore, DPM-EPBEM uses quadratic interpolation to find the displacements at nodes which do not coincide with spots.
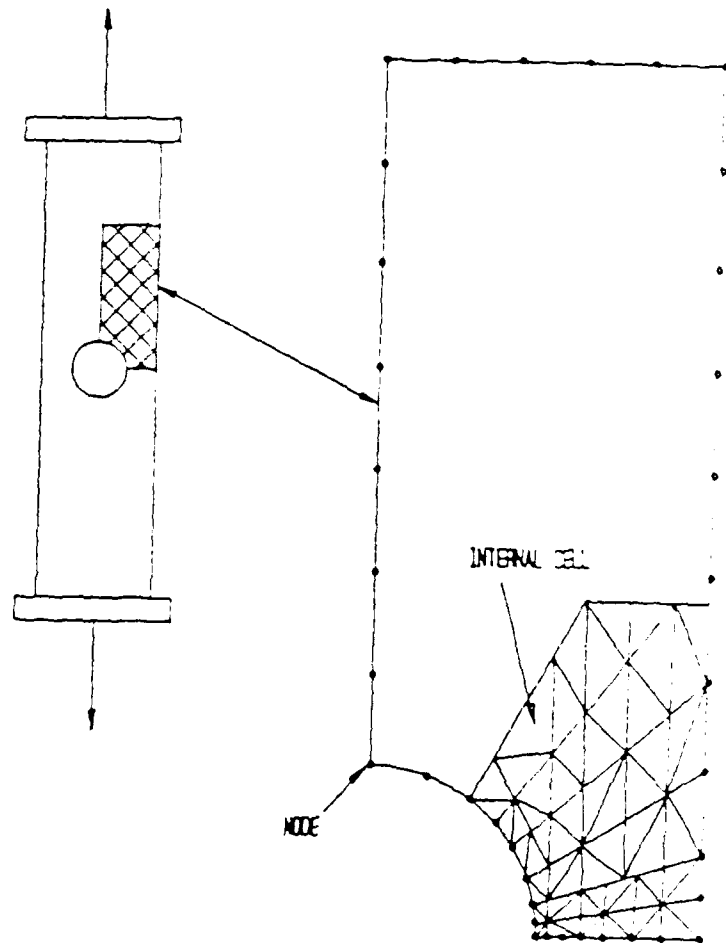
Figure 23.   Schematic of the spot locations on the perforated strip.   .
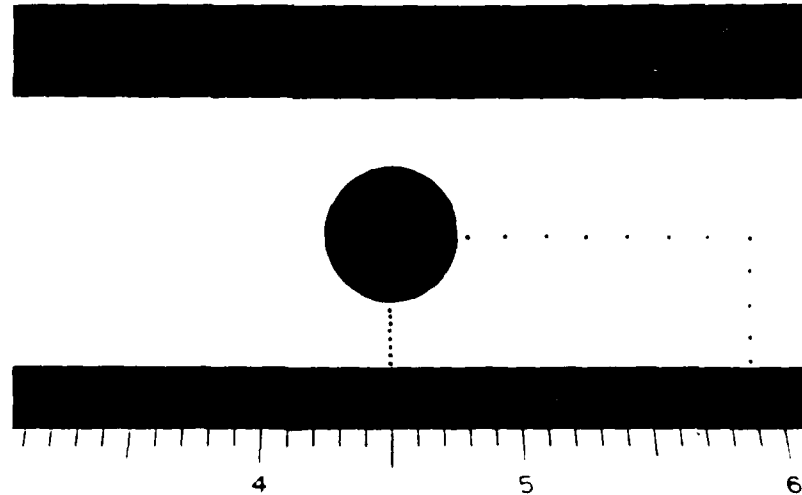
Figure 24.   Photograph of the spots applied to the
perforated strip.

The homogeneous, isotropic hardening option (von Mises
yield condition) and two-dimensional, four point,
isoparametric plate elements (two degrees of freedom) are
used in the finite element solution to this problem. ANSYS
follows an initial stress [96] solution procedure, modelling
the stress-strain curve with five piecewise linear segments.
One symmetric quarter of the specimen is modelled
(Figure 26) and is loaded with 50 psi traction increments,
added to the initial traction of 3000 psi. The load steps
are applied until a value of 6000 psi is reached. The DFM-
EPBEM, ANSYS, and Theocaris' stress concentration factors at
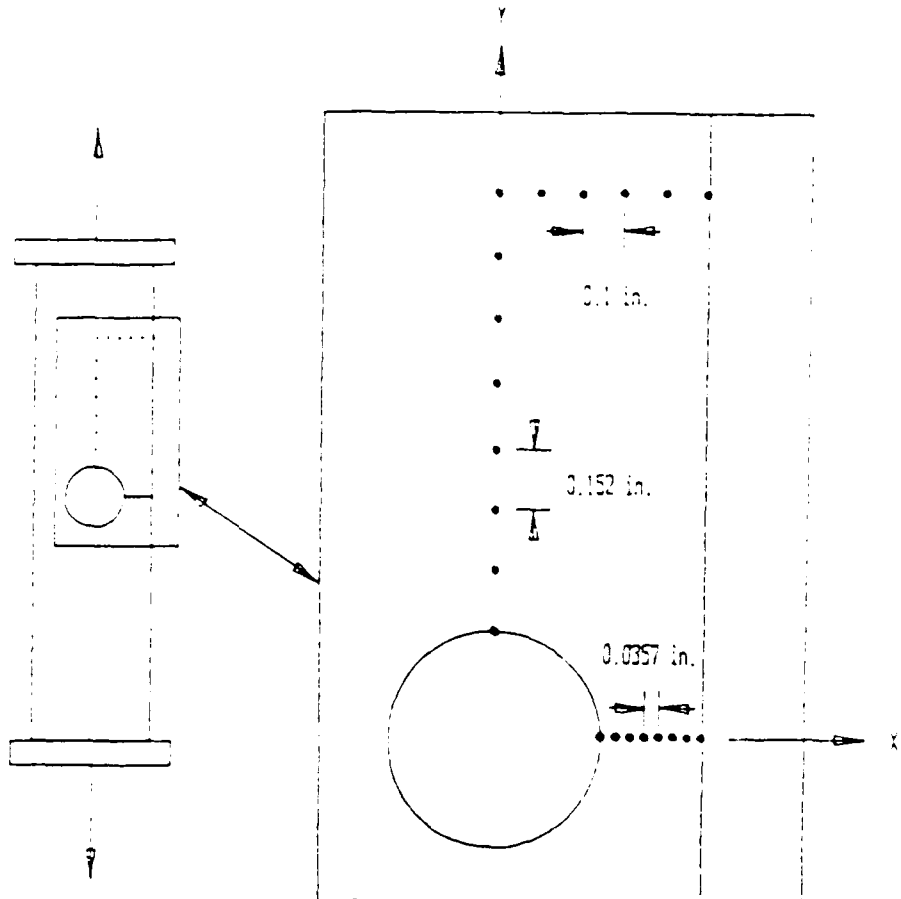
Figure 25.   Boundary element domain discretization of
the perforated strip.
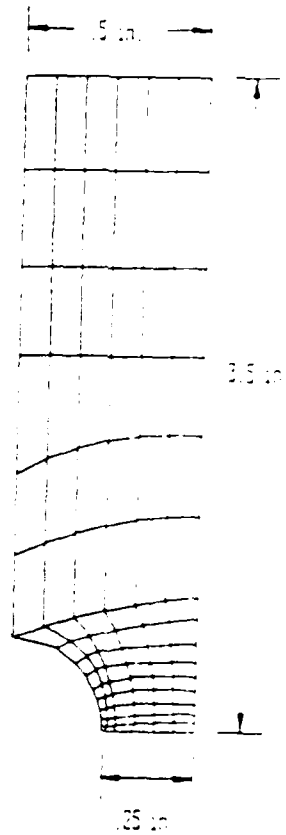
Figure 26.   Finite element grid for the perforated
strip.

(x=0.25 in., y=0.0 in.) as a function of load step are given

in Figure 27.   From here on, the stress concentration factor

(SCF) is defined as the current y-component of stress

divided by the applied stress.   The finite element and DPM-

EPBEM results compare well, with DPM-EPBEM exhibiting one

larger excursion at the sixth load step.   No immediate
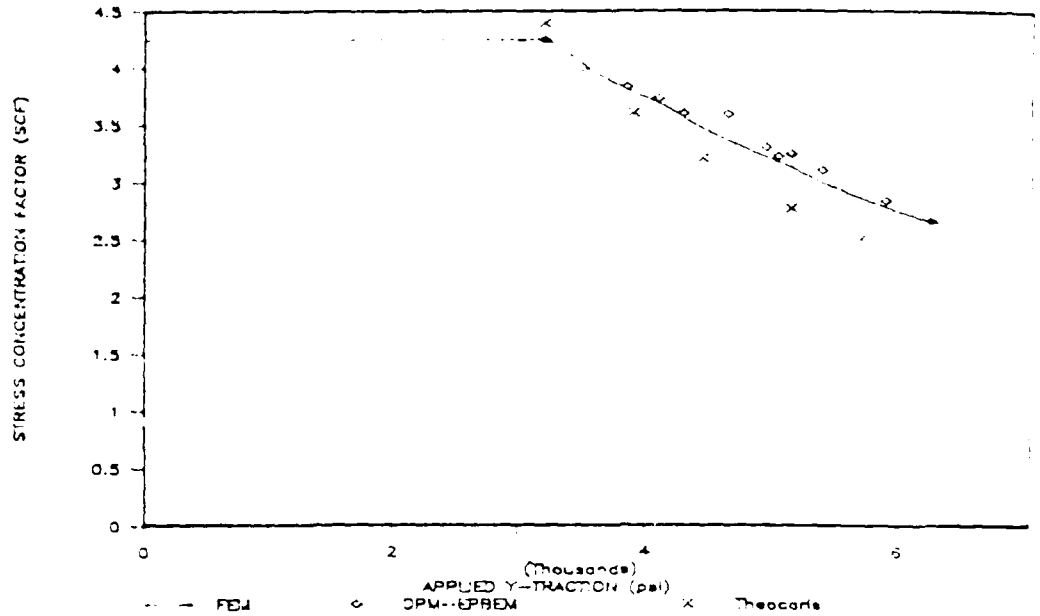
Figure 27. Plot of stress concentration factor versus load step for the perforated strip.

explanation for this anomaly is apparent. Since the next increment's result does not seem to be affected, one might presume that some grip slippage had occurred.

Perhaps even more comforting are the experimental points produced by Theocaris and Marketos [95]. The material they tested was also an aluminum alloy. It exhibited a similar uniaxial stress-strain curve to Figure 21 with a higher yield strength (34,500 psi). Although the SCF curves are not identical, which is not to be expected, the purely experimental, hybrid and purely numerical behaviors are remarkably similar.

The difference in the response could be caused by one of many reasons. Theocaris and Marketos use a bi-linear approximation of the uniaxial stress-strain curve in their analysis whereas the DPM-EPBEM uses a combination of Ramberg-Osgood and linear fits. Theocaris and Marketos make no mention of whether they did or did not anneal their specimens, nor do they discuss their loading apparatus in any detail. Therefore, one would not necessarily expect perfect agreement.

Other interesting information produced by the hybrid technique is the load-displacement curve for (x=0.0 in., y=.25 in.) which is given in Figure 28. The load-displacement results mimic (in shape) the load-maximum strain curves reported by Zienkiewicz [97]. Although not definitive, they certainly are supportive of DPM-EPBEM reliability. In his study, Zienkiewicz used the material properties reported by Theocaris and Marketos.

A final plot, Figure 29, demonstrates the extent of the plastic zone by giving the SCF at various radial locations from the root of the hole (for t_y=6000 psi). The slight inflections at x=0.4 in. and x=0.275 in. are apparent in all of the graphs provided by Theocaris and Marketos [95] and are therefore reassuring.
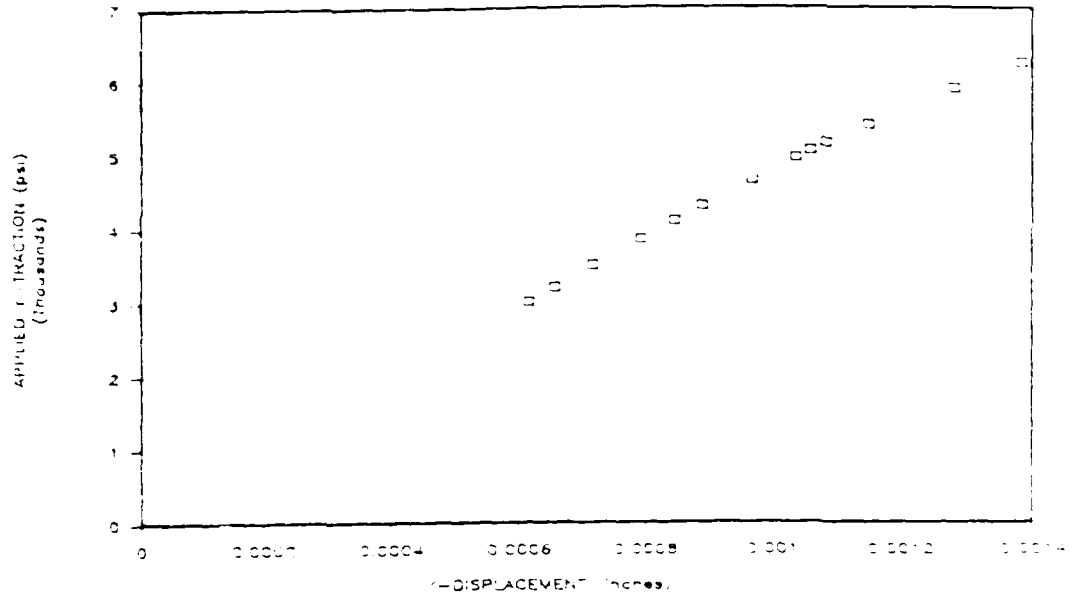
Figure 28. Load-displacement plot for (x=0.,y=.25) on the perforated strip.
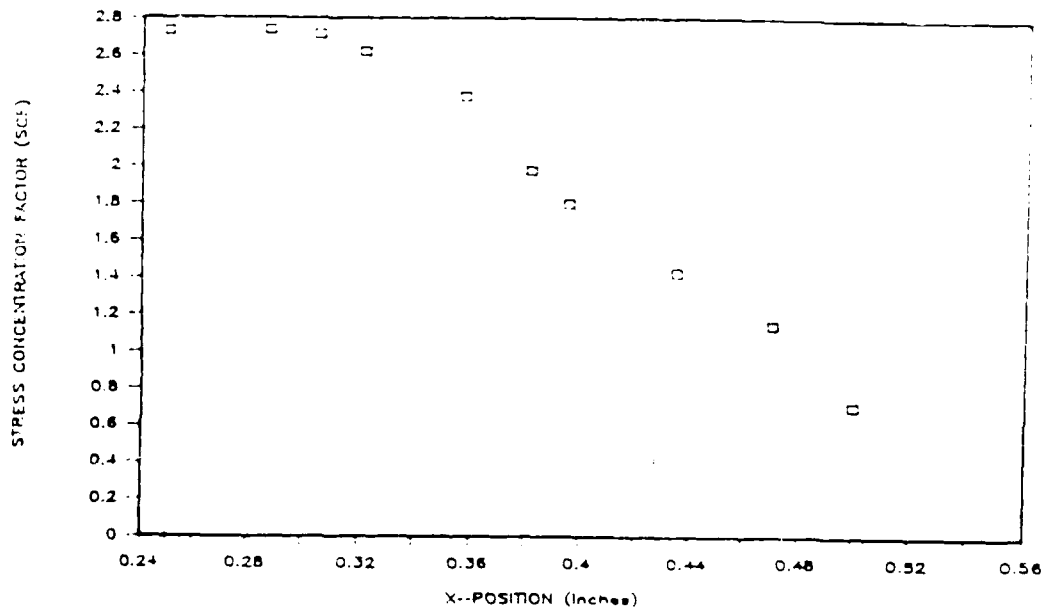
Figure 29. Plot of stress concentration factor versus x-position on the perforated strip.

IV.6   V-notched Specimen Tensile Test

The correlation between DPM-EPBEM, finite element
analysis and the purely experimental results establish a
footing from which a more complex problem can be approached.
The concluding experiment attempts to subject the hybrid
technique to a stress state truly representative of common
engineering problems, a notched tensile specimen [98].
This geometry (Figure 30) produces high stress gradients
localized near the root of the notch with a complex stress
field in the surrounding material [99]. It should be noted
that there is a small machine-induced rounding of the notch
root; therefore, the notch cannot be considered sharp in
the ideal sense. Once again, the ANSYS finite element code
and selected published results are compared to those
produced by the DPM-EPBEM hybrid technique.

As before, the spots are positioned according to
Figure 30 and displayed in Figure 31. A sketch of the
boundary element grid can be found in Figure 32 and one of
the finite element grid in Figure 33. Again, the
homogeneous, isotropic hardening option and two-
dimensional, four point isoparametric elements are used in
the finite element solution of this problem.

Both the SCF vs load increment (Figure 34) and the load
-displacement curve for (x=0.0 in. ,y=.47 in.) (Figure 36)
are provided for evaluation of the performance of DPM-EPBEM.
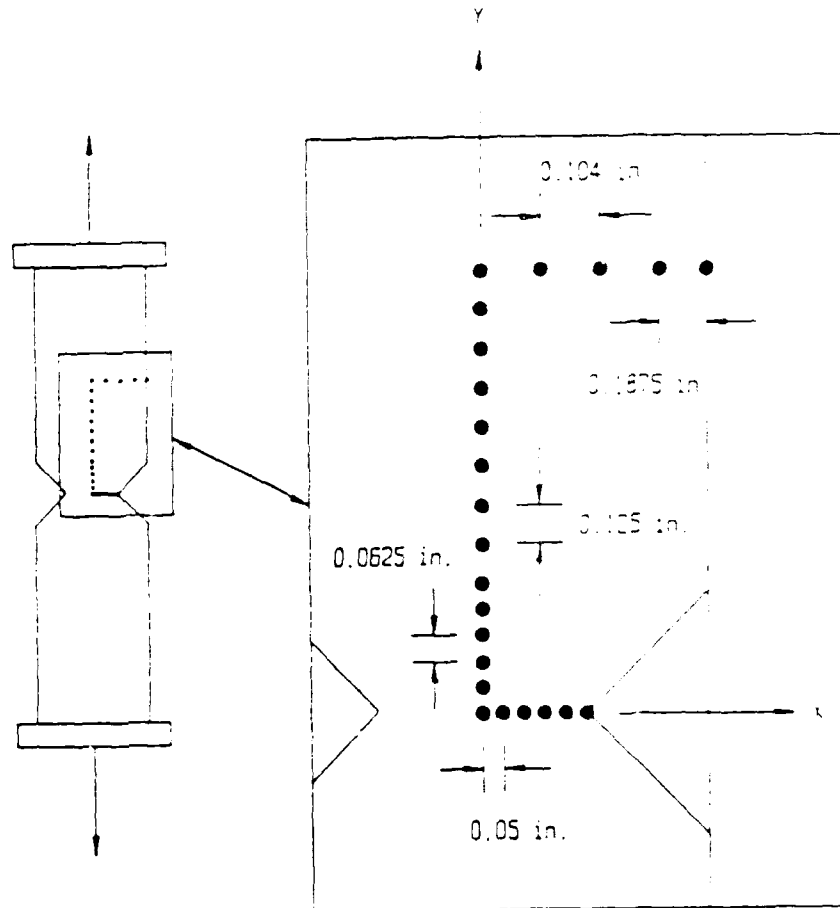
Figure 30.   Schematic of the spot locations on the
V-notched tensile specimen.

The finite element stress concentration factor plot is calculated by first applying an end load of 2000 psi, and by then adding load increments of 50 psi until reaching a value of 5400 psi. In Figure 34, the hybrid and FEM results differ markedly. The first point of deviation is at first yield. DPM-EPBEM predicts that the first yield will occur at an applied traction of 3800 psi, whereas ANSYS predicts
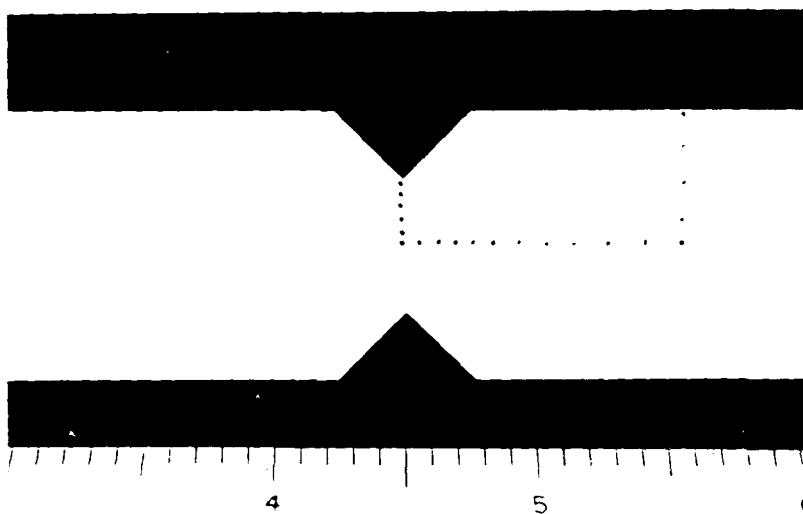
Figure 31. Photograph of the spots applied to the
V-notched tensile specimen
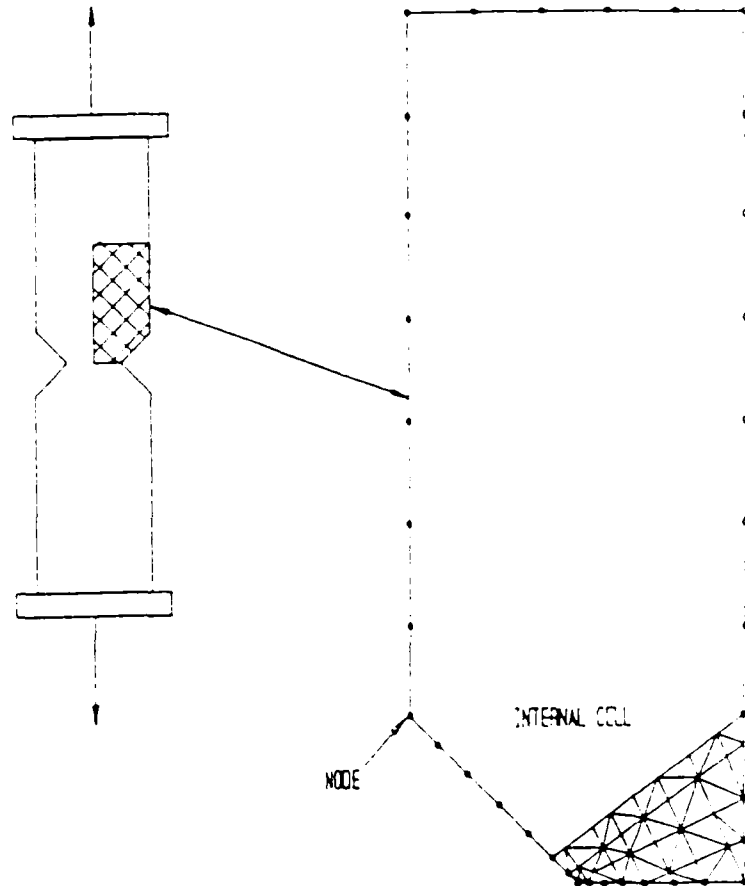
Figure 32. Boundary element domain dicretization of
the V-notched tensile specimen.

the first yield at 3100 psi. One cannot say which is a

better solution but domain discretization does have an

impact on the comparison. If the notch is perfectly sharp,

then plastic deformation initiates when the first load is

applied. The deformation field is so localized that many

internal cells placed near the notch tip would be needed to
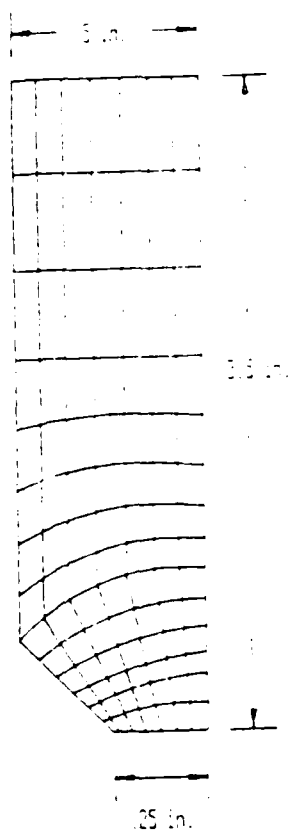
Figure 33. Finite element mesh for the grid for the
V-notched tensile specimen.

discern the motion. The stress calculated at each cell is

an average representation. Therefore, at the notch root,

the larger cells produce smaller average values. A

comparison shows that the finite element grid has three less

cells near the notch root than does the boundary element

grid; therefore, it is reasonable to expect that the first

yield predictions by BEM and FEM will be different.

Experimental error also contributes the different initial
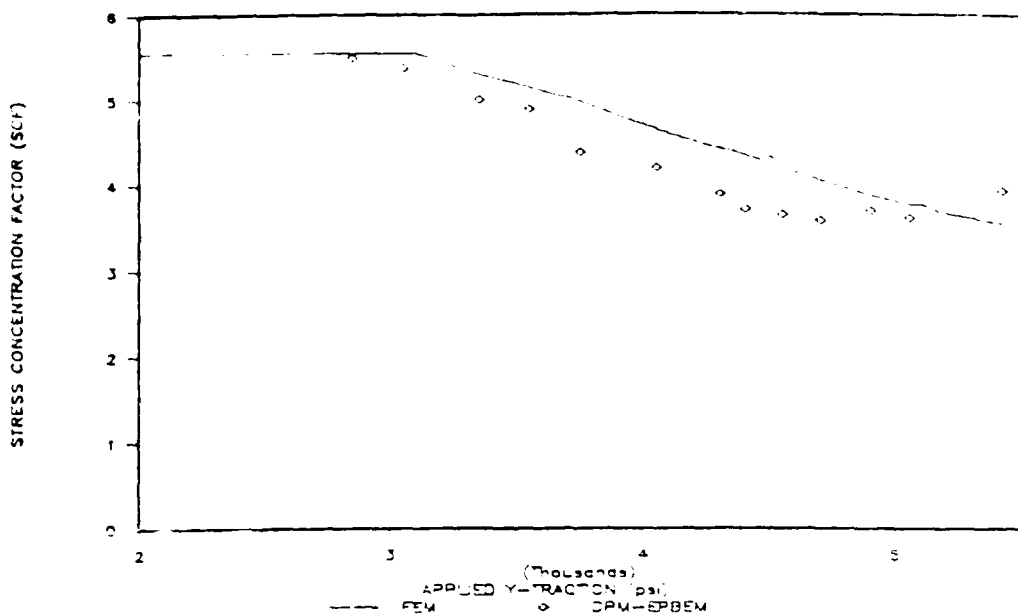
Figure 34. Plot of stress concentration factor versus
load step for the V-notched tensile
specimen.

yield predictions of DPM-EPBEM and FEM. The erratic hybrid

SCF curve suggests that some of the DPM displacements may be

in error. If this is so, then the early increments would

equally be in error. Regardless of the reasons for the

difference in the predictions, the qualitative similarity is

apparent with the quantitative results differing at most by

14.9%.

Other important considerations deal primarily with the

difference between the ideal loading conditions in the

numerical simulation and the actual loading conditions in

the hybrid technique. Examination of the post yield

specimen (Figure 35) indicates that yield did not occur
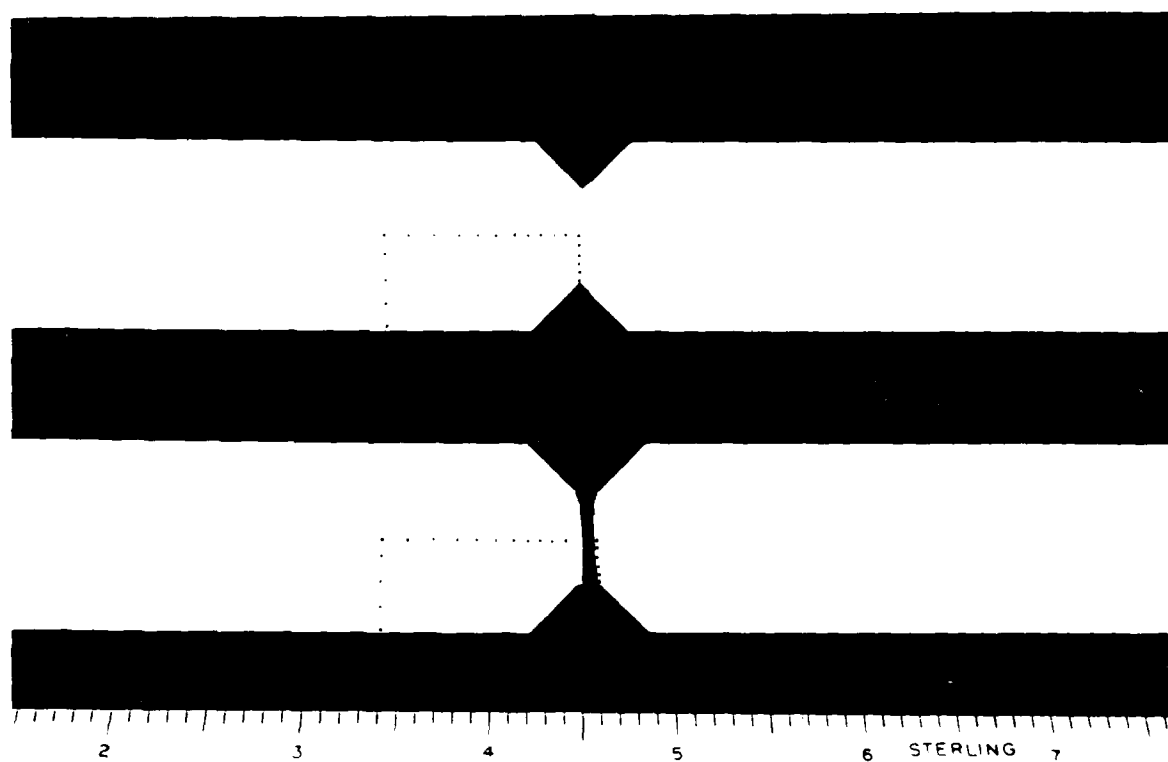
Figure 25. Photograph of the V-Notched Tensile
            Specimen Before Loading and After Failure

simultaneously at both notch roots. This, in turn, implies that the specimen was not perfectly aligned in the MTS grips, precipitating a non-symmetric stress state. In such a case as this, one cannot expect the FEM solution to duplicate the experimental results.

Although no comprehensive experimental investigation of the V-notched test specimen is available, inferences from results presented by several previous experimental and numerical studies lend credence to the results presented here. The load displacement curve given in Figure 36 qualitatively compares well with a similar numerical curve reported by Telles [18] (page 171) and with the experimental curve reported by Findley and Drucker [100] (1/16 inch specimens). In both cases, the material is an aluminum alloy which is different from the material used here. Additionally, the aspect ratios and the net cross sectional areas of their specimens differ from those used in the present experiments. Taking these facts into consideration and the fact that EPBEM reached its upper performance limit before the plastic limit load, Figure 36 exhibits the characteristic linear load-displacement curve in the pre-limit load regime. Linear behavior from a plastically deforming body may seem contradictory, but in this case it is reasonable. During the early stages of plastic deformation (as is the case with DPM-EPBEM) the plastic zone is localized in the region near the root of the notch. The
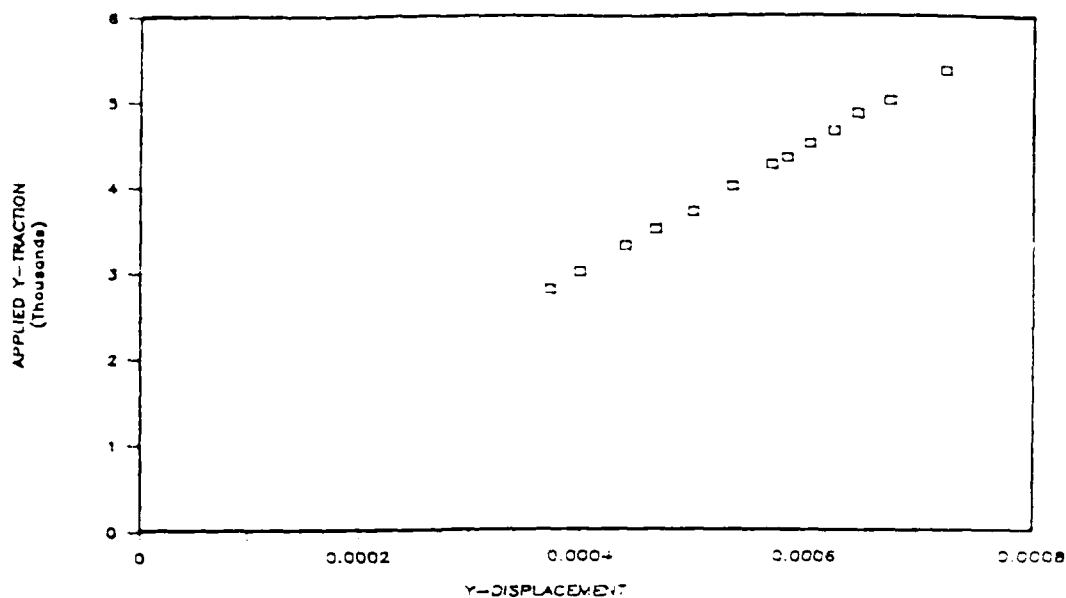
Figure 36. Load-displacement plot for (x=0,y=.46) on the V-notched tensile specimen.
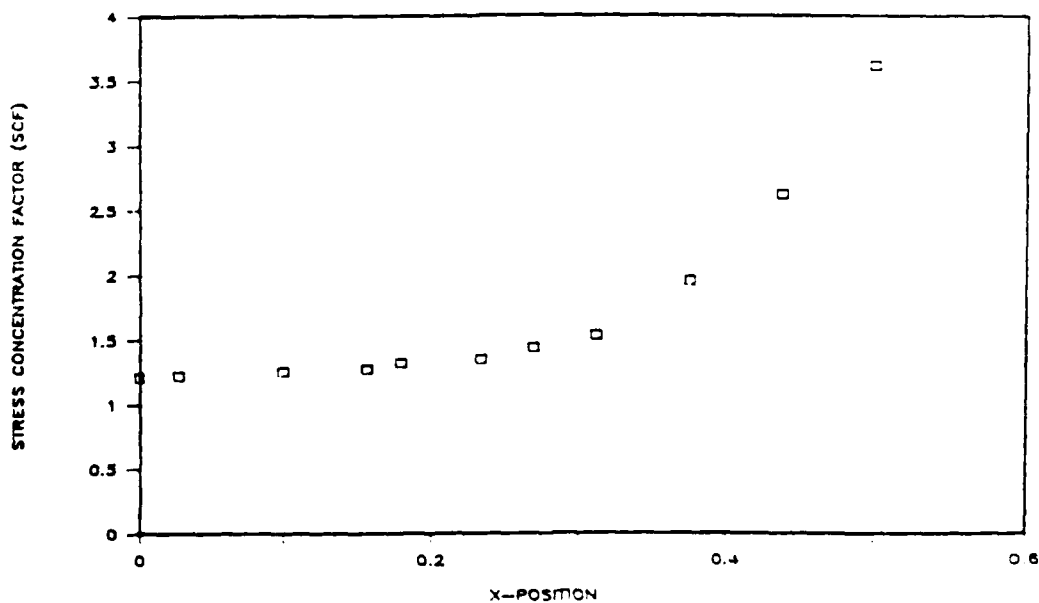
Figure 37. Plot of stress concentration factor versus x-position on the V-notched tensile specimen.

surrounding elastic material confines the plastic zone and effectively stems any large plastic deformation. The regions away from the root are essentially unaware of the plastic flow until the loads are high enough to produce substantial redistribution of the internal stress state of the specimen and, in turn, a larger plastic flow [100].

Finally, the stress concentration factor along the $y=0$ axis (Figure 37) follows the expected course by increasing as one moves closer to the root. The EPBEM upper performance limit (5400 psi) prevents a fully developed plastic zone and hence a flattening out of the SCF curve is not present. The SCF versus position plot is taken for an applied load of 4700 psi, a load at which the plastic zone is still confined to the notch root.

SECTION V

CONCLUSIONS

The two-dimensional numerical-experimental hybrid technique described herein combines context-free syntactic pattern recognition (DPM) and elastic-plastic boundary element methods (EPBEM) to produce a useful, non-destructive stress analysis tool. Within a certain load range, all of the presented DPM-EPBEM results compare well with finite element and purely experimental (where available) solutions. The DPM-EPBEM solution for the V-notched tensile specimen exhibits a more erratic response than the responses of the other two experiments. Since the V-notched tensile specimen represents a state of stress that is as complex as one would expect to encounter in engineering problems, an understanding of the results of that test is paramount to evaluating DPM-EPBEM's usefulness as a stress analysis tool.

DPM-EPBEM works well in load ranges where rigid body motion is negligible when compared to the displacements produced by distortion. Rigid body motion in the initial

stages of loading (approximately 90% of the proportional limit) degrades the accuracy of the DPM-EPBEM hybrid technique. This lower accuracy limit can be improved by incorporating rigid body motion compensation in DPM or EPBEM.

In instances when DPM-EPBEM returns questionable results, a possible question might be raised about how to guarantee that the applied spots are in the exact locations as specified in Figures 49, 53 and 60. The accuracy of the spot application technique described in Section IV is limited by human error. In most cases, the accuracy of the spot location technique is approximately ±.001 inch. Surprising as it may seem, mirroring the schematics is not that critical. The boundary element code does receive displacement information from DPM, but it also receives and stores the locations of the spot centroids in the undeformed image. Using this information, DPM-EPBEM interpolates (or extrapolates as the case may be) the displacement information to the BEM node locations. This is not to say that errors are not introduced by misalignment of the spots. If the spots are to be located along a horizontal line, then misalignment in the vertical direction can play a significant role. However, DPM-EPBEM is very forgiving with respect to spot placement errors.

Given that the spots are perfectly aligned, the ability of DPM to measure the displacements accurately is certainly paramount to the success of the hybrid technique. In the images used in this investigation, typical values for signal-to-noise ratio, gray level difference and displacement resolution are 200, 100 pixels and 0.0001 inch, respectively. In many situations there are regions in the tested specimens where this resolution is insufficient. As an example, the stress concentration factors for the perforated strip and the V-notched tensile specimens are calculated at the boundary of the respective cutout roots. Therefore, the DPM displacement error plays an important role in the SCF results. Both cases include localized plastic zones and the same nominal dimensions. Because of these localized regions, one anticipates that the displacement in the region near the cutout roots governs the accuracy of the DPM displacements. Minor displacement errors away from the cutout roots do not have the influence of displacement errors in the plastic zone. The plots in Figures 57 and 64 follow the above reasoning; if the resolution for both experiments is the same, then only regions of small displacements (on the order of the resolution limit) can account for the difference in the behavior of the SCF plots. This conclusion immediately draws attention to the displacement in the regions surrounding the cutout roots. The plastic flow in the

perforated strip is not as confined as it is in the V-notch
specimen. Therefore, the displacement at the root of the
circular cutout experiences larger and more measurable
displacements. The displacements near the V-notch are much
more confined by the surrounding elastic region which holds
the displacements nearer to the resolution limit of DPM. As
a result, the SCF plot for the V-notch specimen is much more
erratic.

One should note that the specimens used in the
evaluation of DPM-EPBEM are smaller (nominal dimensions are
one inch wide, nine inches tall and .0625 inch thick) than
one would expect to encounter in many true engineering
problems. The displacements in larger specimens will be
bigger and more measurable than the displacements
encountered here. This argument holds for localized plastic
zones; they too will encompass larger areas, providing more
sizable displacements. Therefore, in larger structures, the
DPM-EPBEM is less likely to encounter the resolution limit
of DPM. Avenues for improving the DPM resolution are
available for problems dictating measurements on the order
of the resolution limit. The interpolation of the
displacement information from spot locations to node
locations has the effect of smoothing out the influence of
the poor data near the roots of the cutouts. This suggest
that smoothing techniques tailored to these types of
problems may be useful. The real solution, however, is to

improve the resolution of DPM. This can be accomplished by increasing the calibration constants through magnification or with better hardware, or by compensation for system errors.

Another area which needs improvement deals with the elastic-plastic boundary element method. The convergence of the initial strain elastic-plastic boundary element solution is sensitive to load increment step size. As seen in the experiments presented in Section IV, it is not always possible to apply the loads in such way as to stay within the realm of incremental plasticity and thereby guarantee convergence. Therefore a solution procedure which is less sensitive to increment size would be more desirable. Fortunately, the initial stress solution approach has just this quality [101]. It is anticipated that an initial stress solution procedure would greatly enhance the load range in which this hybrid technique is applicable.

The evaluation of DPM-EPBEM is given in the above paragraphs so that the limitations of this technique can be understood and so areas of further research can be pinpointed. But even in its present stage of development, the hybrid experimental-numerical procedure described in this report is a useful stress analysis tool. The good results presented in Section IV are one indication of the promise that the DPM-EPBEM procedure holds. A second indication of the promise of this technique is that it is

fully automated. Finally, the equipment required to produce a hybrid method like the one described is standard at most engineering and research facilities. By incorporating the above suggestions, the displacement pattern matching, elastic-plastic boundary element hybrid method can be shaped to provide good solutions over an even wider load range.

APPENDIX

The two volume integrals encountered in elasto-plastic boundary element methods appear in the boundary constraint equation (Equation II-15) and the interior strain equation (Equation II-40). Here these integrals are identified and their semi-numerical integration is described.

The constraint equation volume integral is written as

$$\Delta\Sigma_{ijk} = \int_{\bar{V}} S^{*}_{ijk}(r)\,dV$$

where

$$S^{*}_{ijk}(r) = \frac{C_1}{r}\,[C_2(\delta_{ij}r,_k + \delta_{ik}r,_j - \delta_{jk}r,_i) + r,_i r,_j r,_k]\quad (A-1)$$

with

$$C_1 = -\frac{1}{4\pi(1-\nu)}\quad,$$

$$C_2 = (1-\nu)\quad,$$

$$r_i = x_i - \xi_i \quad\text{and}$$

$$r,_i = \frac{\partial r}{\partial x_i}\quad.$$

To change from plane strain to plane stress replace ν by $\frac{\nu}{1+\nu}$. As described in Section II, the volume integral is evaluated over each triangle (Figure 8 and 9) and algebraically summed to find the integral over each interior cell. It is instructive to show this integration over a representative triangle so as to understand its numerical attributes and shortcomings.
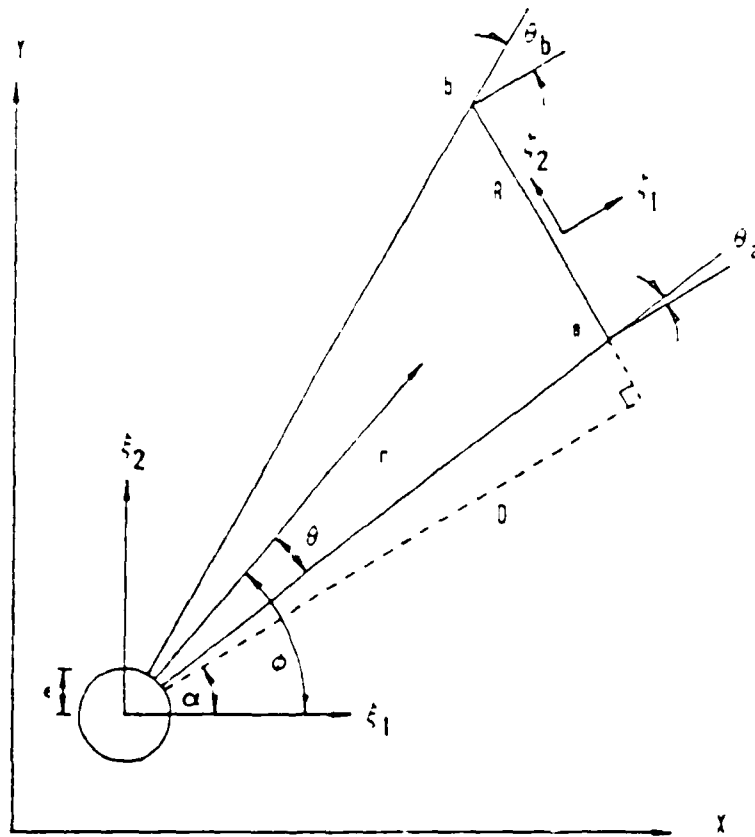

Figure 38. Coordinate system for the integration over an arbitrary triangular cell.

A transformation to cylindrical coordinates simplifies the integration.

$$\Delta\Sigma_{ijk}(r) = \lim_{\epsilon \to 0} \int_{\phi_a}^{\phi_b} \int_{\epsilon}^{R(\phi)} S^*_{ijk}(r,\phi)\, r\, dr\, d\phi \qquad (A-2)$$

where r, ϕ, θ_a, ϕ_b, $R(\phi)$ and Σ_{ijk} are defined in Figure 38. The integration is carried out with respect the line segment, D, perpendicular to $R(\phi)$. This introduces the new coordinate system ζ_1, ζ_2. By defining the derivatives of r in cylindrical coordinates, Σ_{ijk} is properly recast.

$$r_{,j} = \frac{\partial r}{\partial x_i} = \frac{\partial r}{\partial \zeta_1}\frac{\partial \zeta_1}{\partial x_i} + \frac{\partial r}{\partial \zeta_2}\frac{\partial \zeta_2}{\partial x_i} \qquad (A-3)$$

As seen from Figure 38, $\dfrac{\partial r}{\partial \zeta_1} = \cos\phi$, $\dfrac{\partial r}{\partial \zeta_2} = \sin\phi$, $\dfrac{\partial \zeta_1}{\partial x_i} = e_{1i}$

and $\dfrac{\partial \zeta_2}{\partial x_i} = e_{2i}$; where e_{ij} are the direction cosines between the x and ζ coordinate systems. Therefore,

$$r_{,i} = \cos\phi\, e_{1i} + \sin\phi\, e_{2i}, \qquad (A-4)$$

and combining Equations (A-1), (A-2) and (A-4) gives

$$\Delta\Sigma_{ijk} = C_1 C_2 \int_{\phi_a}^{\phi_b} R(\phi)\delta_{ij}(\cos\theta\, e_{1k} + \sin\phi\, e_{2k})\, d\phi$$

$$+ C_1 C_2 \int_{\phi_a}^{\phi_b} R(\phi)\delta_{ik}(\cos\theta\, e_{1j} + \sin\phi\, e_{2j})\, d\phi$$

$$(A-5)$$

$$- C_1 C_2 \int_{\phi_a}^{\phi_b} R(\phi)\delta_{jk}(\cos\theta\, e_{1i} + \sin\phi\, e_{2i})\, d\phi$$

$$+ 2C_1 \int_{\phi_a}^{\phi_b} [R(\phi)(\cos\phi \, e_{1i} + \sin\phi \, e_{2i})(\cos\phi \, e_{1j} + \sin\phi \, e_{2j})$$

$$+ (\cos\phi \, e_{1k} + \sin\phi \, e_{2k})] d\phi.$$

From the geometry shown in Figure 38, $\phi = \theta + \alpha$, $d\phi = d\theta$ and $R(\phi) = D/\cos\phi$, and therefore the integral, ψ_{ijk} is

$$\psi_{ijk} = DC_1C_2((e_{1k}\delta_{ij} + e_{1j}\delta_{ik} - e_{1i}\delta_{jk})$$

$$+ \tan\theta \, (e_{2k}\delta_{ij} + e_{2j}\delta_{ik} - e_{2i}\delta_{jk}))$$

$$+ DC_2(2\cos^2\theta \, e_{1i}e_{1j}e_{1k}$$

$$+ 2\cos\phi\sin\phi \, (e_{2i}e_{1j}e_{1k} + e_{1i}e_{2j}e_{1k} + e_{1i}e_{1j}e_{2k})$$

$$+ 2\sin^2\theta \, (e_{2i}e_{1j}e_{2k} + e_{1i}e_{2j}e_{2k} + e_{2i}e_{2j}e_{1k}) \qquad (A-6)$$

$$+ 2\sin^2\theta\tan\theta \, e_{2i}e_{2j}e_{2k}).$$

Upon integration Equation (A-5) reduces the integral of S_{ijk}^{*} over an arbitrary triangle.

$$\Delta\Sigma_{ijk} = C_1C_2D((e_{1k}\delta_{ij} + e_{1j}\delta_{ik} - e_{1i}\delta_{jk})I_1$$

$$+ (e_{2k}\delta_{ij} + e_{2j}\delta_{ik} - e_{2i}\delta_{jk})I_2) + DC_2 e_{1i}e_{1j}e_{1k}I_3$$

$$+ DC_2(e_{2i}e_{1j}e_{1k} + e_{1j}e_{2j}e_{1k} + e_{1i}e_{1j}e_{2k})I_4$$

$$+ DC_2(e_{2i}e_{1j}e_{2k} + e_{1i}e_{2j}e_{2k} + e_{2i}e_{2j}e_{1k})I_5$$

$$+ DC_2 e_{2i}e_{2j}e_{2k}I_6, \qquad (A-7)$$

where

$$I1 = \int_{\theta_a}^{\theta_b} d\theta = \theta_b - \theta_a \quad ,$$

$$I2 = \int_{\theta_a}^{\theta_b} \tan\theta \, d\theta = -\ln(\frac{\cos\theta_b}{\cos\theta_a}) = \ln(\frac{r_b}{r_2}) \quad ,$$

$$I3 = \int_{\theta_a}^{\theta_b} 2\cos^2\theta \, d\theta = (\theta_b - \theta_a) + \frac{1}{2}(\sin 2\theta_b - \sin 2\theta_a) ,$$

$$I4 = \int_{\theta_a}^{\theta_b} 2\cos\theta \sin\theta \, d\theta = \sin^2\theta_b - \sin^2\theta_a \quad ,$$

$$I5 = \int_{\theta_a}^{\theta_b} 2\sin^2\theta \, d\theta = (\theta_b - \theta_a) + \frac{1}{2}(\sin 2\theta_b - \sin 2\theta_a)$$

$$I6 = \int_{\theta_a}^{\theta_b} 2\tan\theta \sin^2\theta \, d\theta = 2\ln(\frac{r_b}{r_a}) + \cos^2\theta_b - \cos^2\theta_a$$

The volume integral associated with the total strain
equation is simply the derivative of Equation (A-7) (see the
development of Equation II-40), that is

$$\Delta E_{\ell ijk} = \frac{\partial}{\partial \xi_\ell}(\Delta \Sigma_{ijk}). \qquad (A-8)$$

Here the derivative is taken with respect to the load point
If ξ is perturbed then D and its associated angles change;
C_1, C_2 and e_{ij} remain fixed. Evaluating Equation (A-8) is
now reduced to finding

$$I'_{1\ell} = \frac{\partial}{\partial \xi_\ell}(DI_i) \quad \text{where } \ell = 1, 2, \ldots 6,$$

which by the chain rule expands to

$$I'_{1\ell} = \frac{\partial D}{\partial \xi_\ell} I_i + \frac{\partial I_i}{\partial \theta} \frac{\partial \theta}{\partial \xi_\ell} D \ . \tag{A-9}$$

The first term $\frac{\partial D}{\partial \xi_\ell} = -e_{1\ell}$ and $\frac{\partial \theta}{\partial \xi_\ell}$ in the second term is

evaluated as follows:

$$\theta = \tan^{-1} \left(\frac{\xi_2}{\xi_1}\right) - \alpha \ ,$$

$$\frac{\partial \theta}{\partial \xi} = - \frac{\xi_2}{R} \ , \tag{A-10}$$

but $\xi_2 = R\sin(\theta + \alpha)$, after expanding and substituting into Equation (A-10)

$$\frac{\partial \theta}{\partial \xi_1} = - \frac{\sin\theta\cos\alpha - \cos\theta\sin\alpha}{R} \ .$$

similarly

$$\frac{\partial \theta}{\partial \xi_2} = - \frac{\cos\theta\cos\alpha - \sin\alpha\sin\theta}{R} \ .$$

By making use of the direction cosines

$$\frac{\partial \theta}{\partial \xi_\ell} = - \frac{e_{2\ell}\cos\theta - e_{1\ell}\sin\theta}{R} \ .$$

Now, by substituting the above results into Equation (A-9) ΔE_{1ijk} can be written for a representative triangle

$$\Delta E_{\ell ijk} = C_1 C_2 (e_{1k}\delta_{ij} + e_{1j}\delta_{ik} - e_{1i}\delta_{jk}) I_1'$$
$$+ C_1 C_2 (e_{2k}\delta_{ij} + e_{2j}\delta_{ik} - e_{2i}\delta_{jk}) I_2'$$
$$+ C_2 e_{1i} e_{1j} e_{1k} dI_3' + C_2 (e_{2i} e_{1j} e_{1k}$$
$$+ e_{1i} e_{2j} e_{1k} + e_{1i} e_{1j} e_{2k}) I_4'$$
$$+ C_2 (e_{2i} e_{1j} e_{2k} + e_{1i} e_{2j} e_{2k} + e_{2i} e_{2j} e_{1k}) I_5'$$
$$+ C_2 e_{2i} e_{2j} e_{2k} I_6' ,$$

where

$$I_1' = -(\theta_b - \theta_a) e_{11} + (\eta_b - \eta_a) ,$$

$$I_2' = \eta_b \tan\theta_b - \eta_a \tan\theta_a - \ln(\frac{r_b}{r_a}) e_{1\ell} ,$$

$$I_3' = 2\eta_a \cos^2\theta_a - 2\eta_b \cos^2\theta_b$$
$$- ((\theta_b - \theta_2) + \sin\theta_b \sin\theta_a - \cos\theta_a \sin\theta_a) e_{1\ell} ,$$

$$I_4' = 2\eta_b \sin\theta_b \cos\theta_b - 2\eta_a \sin\theta_a \cos\theta_a$$
$$- (\sin^2\theta_b - \sin^2\theta_a) e_{1\ell}$$

$$I_5' = 2\eta_b \sin^2\theta_b - 2\eta_a \sin^2\theta_a - (\theta_b - \theta_a) e_{1\ell}$$
$$+ (\sin\theta_b \cos\theta_b - \sin\theta_a \cos\theta_a) e_{1\ell}$$

and

$$I_6' = 2\eta_b \tan\theta_b \sin^2\theta_b - 2\eta_a \tan\theta_a \sin^2\theta_a - 2\ln(\frac{r_a}{r_a}) e_{1\ell}$$
$$- (\cos^2\theta_b - \cos^2\theta_a) e_{1\ell};$$

where η_a and η_b are $D \frac{\partial \theta}{\partial \xi_\ell}$ evaluated at points a and b, respectively.

REFERENCES

1. Durelli, A. J., APPLIED STRESS ANALYSIS, Prentice-Hall, Englewood Cliffs, N. J., 1967.

2. Frocht, M.M., PHOTOELASTICITY, Vol. 1, Wiley, New York, 1941.

3. Kobayashi, A. S., "Hybrid Experimental-Numerical Stress Analysis," in HANDBOOK ON EXPERIMENTAL MECHANICS (A. S. Kobayashi ed.), Prentice-Hall, Englewood Cliffs, N. J., pp. 739-768, 1987.

4. Seguci, Y, Tomita, Y., and Watanabe, M. "Computer-Aided Fringe-Pattern Analyzer--A Case of Photoelastic Fringe," Exp. Mech., 19, 362-370, 1979.

5. Deiz, E., Chamblee, D., Swinson, W., and Turner, J., "Image-Processing Techniques in Laser Speckle Photography with Application to Hybrid Stress Analysis," Exp. Mech., 26, pp. 230-238, 1986.

6. Liu, J. C., Sutton, M. A., Chao, Y. J., Peters, W. F., and Ranson, W. F., "A Study of a Consistent Two-Dimensional Boundary Integral Equation Model for Use With Digital Correlation Displacement Measurements," Proc. 10th U.S. Nat. Cong. of Appl. Mech., Austin, 1986.

7. Jaswon, M. A.,"Integral Equation Methods in Potential Theory. I," Proc. Roy. Soc., 273, Ser. A, 1963.

8. Rizzo, F.J. "An Integral Equation Approach To Boundary Value Problems of Classical Elastostatics," Quart. Appl. Math., 25, pp. 83-95, 1967.

9. Brebbia, C. A., Telles, J. F. C., and Wrobel, L. C., BOUNDARY ELEMENT METHODS: THEORY AND APPLICATIONS, Springer-Verlag, New York, 1984.

10. Moslehy, F. A., and Ranson, W. F., "Laser Speckle Interferometry and Boundary Integral Techniques in Experimental Stress Analysis," in DEVELOPMENTS IN THEORETICAL AND APPLIED MECHANICS, Vol. X (J. E. Stoneking, Ed.), Chattanooga, Tenn., Univ. of Tenn., pp. 473-492, 1980.

11. Umeagukwu, I., Peters, W., and Ranson, W.F.,"The Experimental Boundary integral Method in Photoelasticity," in DEVELOPMENTS IN THEORETICAL AND APPLIED MECHANICS, Vol. XI (T. J.Chung and G. R. Karr, Eds), Huntsville, Ala., Univ. of Ala., pp. 181-191, 1982.

12. Balas, J., Sladek, J., and Drzik, M.,"Stress-Analysis by Combination of Holographic Interferometry and Boundary Integral Method," Exp. Mech. 23, pp.196-202, 1983.

13. Liu, C.,Development of a Consistent Boundary Integral Equation Method for Use with Image Processing Method in Experimental Mechanics, Ph.d. Dissertation, University of South Carolina, Columbia, 1984.

14. Mitsui, Y., and Yoshida, S., Separation of Principal Stresses Using Boundary Element Method, "DEVELOPMENTS IN THEORETICAL AND APPLIED MECHANICS, VOL. XIII (W. F. Ranson and J. M. Biedenbach Eds.), Columbia, S.C., University of South Carolina, pp. 263-268, 1986.

15. Shukla, A., Sadd, M. H. and Saliba, E., Two Dimensional Contact Stress Analysis Using a Hybrid Technique of Photoelasticity and Boundary Element Methods," DEVELOPMENTS IN THEORETICAL AND APPLIED MECHANICS, VOL XIII (W. F. Ranson and J. M. Biedenbach Eds.), Columbia, S. C., University of South Carolina, pp. 590-594, 1986.

16. Swedlow, J., L., and Cruse, T. A., "Formulation of Boundary Integral Equations for Three Dimensional Elastoplastic Flow," Int. Jou. Sol. Struc., 7, pp. 1673-1683, 1971.

17. Riccardella, P. C.,"An Implementation of the Boundary-Integral Technique for Planar Problems of Elasticity and Elasto-Plasticity," Ph.d. Dissertation, Carnegie-Mellon University, Pittsburgh, 1973.

18. Telles, J. F. C., THE BOUNDARY ELEMENT METHOD APPLIED TO INELASTIC PROBLEMS, Springer-Verlag, New York, 1983.

19. Cruse, T. A. and Polch, E. Z.,"Nonlinear Fracture
    Mechanics Analysis With the Boundary Integral Method,"
    Air Force Office of Scientific Research Report,
    Alexandria, Va., AFOSR-TR-85-1072, 1985.

20. Banerjee, P., K., and Butterfield, R., BOUNDARY ELEMENT
    METHODS IN ENGINEERING SCIENCE, McGraw-Hill Book Co.,
    London, 1981.

21. Telles, J. F. C., and Brebbia, C. A., "The Boundary
    Element Method in Plasticity," Proc. 2nd. Sem. on
    RECENT ADVANCES IN BOUNDARY ELEMENT METHODS (C. A.
    Brebbia Ed.), University of Southampton, Southampton,
    pp. 295-317, 1980.

22. Swedlow, J. L., "Character of Equations of Elasto-
    Plastic Flow in Three Independent Variables," Int. Jou.
    Non-Linear Mech., 3, pp. 325-336, 1968, 4. pp. 7, 1969.

23. Fail, R. W., "Pattern Mapping in Plane Motion
    Analysis," Ph.d. Dissertation, University of Florida,
    Gainesville, 1987.

24. Miller, J. A., "Improved Photogrid Techniques for
    Detection of Strain Over Short Gauge Lengths," Proc.
    SESA, 10, pp. 29-34, 1952.

25. Durelli, A. J., and Riley, W. F., "Developments in the
    Grid Method of Experimental Stress Analysis," Proc.
    SESA, 9, pp. 91-100, 1957.

26. Obata, M., Shimada, H., and Kawasaki, A., "Fine-Grid
    Method for Large Strain Analysis Near a Notch Tip,"
    Exp. Mech., 23, pp.146-151, 1983.

27. Obata, M., Shimada, H., and Kawasaki, A., "Embedded
    Fine-Grid Method Applied to Three-Dimensional Stress-
    Intensity-Factor Analysis," Exp. Mech., 25, pp. 8-11,
    1985.

28. Kawasaki, M., Obata, M., and Shimada, H., "Computer-
    Aided Fine-Grid Method for Local-Strain Measurement
    Near a Crack-Tip in 2 1/4Cr-Cr-1 Mo Steel at 773 k,"
    Exp. Tech., 11, pp. 24-27, Aug., 1987.

29. Drucker, D. C., "Variational Principles in the
    Mathematical Theory of Plasticity," Proc. Symp. Appl.
    Math., 8, pp. 7-22, 1958.

30. Greenberg, M. D., APPLICATIONS OF GREEN'S FUNCTIONS IN
    SCIENCE AND ENGINEERING, Prentice-Hall, Inc., Englewood
    Cliffs, N. J., 1975.

31. Sokolnikoff, I. S., MATHEMATICAL THEORY OF ELASTICITY, McGraw-Hill, New York, 1956.

32. Love, A. E. H., A TREATISE ON THE MATHEMATICAL THEORY OF ELASTICITY, Dover Publications, New York, 1927.

33. Muskhelishvili, N. I., SINGULAR INTEGRAL EQUATIONS, Nordoff, Groningen-Holland, 1953.

34. Lachat, J. C., "A Further Development of the Boundary Integral Technique for Elastostatics," Ph.d. Dissertation, University of Southampton, Southampton, 1975.

35. Mendelson, A., and Albers, L. U., "Application of Boundary Integral Equation Method to Elasto-Plastic Problems," in PROC. ASME CONF. ON BIEM, AMD-Vol. 11 (T. A. Cruse and F. J. Rizzo Eds.), ASME, Troy, New York, pp.47-84, 1975.

36. Mukherjee, S., BOUNDARY ELEMENT METHODS IN CREEP AND FRACTURE, Applied Science Publishers, New York, 1982.

37. Martin, J. B., PLASTICITY: FUNDAMENTALS AND GENERAL RESULTS, The MIT Press, Cambridge, Mass., 1975.

38. Chen, W., LIMIT ANALYSIS AND SOIL PLASTICITY, Elsevier Scientific Publishing Company, New York, 1975.

39. Drucker, D. C., "Conventional And Unconventional Plastic Response and Representation," to appear in Appl. Mech. Rev., 1988.

40. Johnson, W., and Mellor, P. B., PLASTICITY FOR MECHANICAL ENGINEERS, D. Van Nostrand Co., Ltd., London, 1966.

41. Koiter, W. T., "General Theorems For Elastic-Plastic Solids," in PROGRESS IN SOLID MECHANICS, Vol. 1, (N. I. Sneddon and R. Hill Eds.), Wiley and Sons, New York, pp. 186-203, 1960.

42. Hill, R., THE MATHEMATICAL THEORY OF PLASTICITY, Oxford University Press, London, 1960.

43. Malvern, L. E., INTRODUCTION TO THE MECHANICS OF A CONTINUOUS MEDIUM, Prentice-Hall, Inc., Englewood Cliffs, N. J., 1969.

44. Drucker, D. C., "A More Fundamental Approach to Plastic Stress Strain Relations," PROC. 1st U. S. NAT. CONG. OF APPL. MECH., pp. 487-491, 1951.

45. Drucker, D. C., "Some Implications of Work Hardening and Ideal Plasticity," Quart. of Appl. Math., 7, no. 4, pp.411-418, 1950.

46. Boresi, A. P., Sidebottom, O. M., Seely, F. B. and Smith, J. O., ADVANCED MECHANICS OF MATERIALS, John Wiley and Sons, New York, 1978.

47. Mukherjee, S., "Thermoviscoplastic Response of Cylindrical Structures Using a State Variable Theory," in MECHANICAL BEHAVIOR OF MATERIALS-PROC. OF IMC 3, Cambridge(K. J. Miller, and R. F. Smith Eds.), Pergamon Press, Oxford, pp. 233-242, 1979.

48. Cruse, T. A. and Polch, E. Z., "Nonlinear Fracture Mechanics Analysis With The Boundary Integral Method," Airforce Office of Scientific Research Report, Alexandria, Va., AFOSR-TR-85-1072, pp. 10-29, 1985.

49. Brebbia, C. A., and Walker, S., BOUNDARY ELEMENT TECHNIQUES IN ENGINEERING, Newnes-Butterworths, Sydney, 1980.

50. Hornbeck, R. W., NUMERICAL METHODS, Prentice-Hall, Englewood Cliffs, N. J., 1975.

51. Sirkis, J. S. "Boundary Element (Integral) Solutions to Heat Conduction Problems," Air Force Office of Scientific Research Report, Alexandria, Va., AFATL-TR-86-90, pp. 1-11, 1986.

52. Mendelson, A. "Boundary Integral Methods in Elasticity and Plasticity," National Aeronautics and Space Administration Report, Huntsville, Ala., NASA TN D-7418, 1973.

53. Mukherjee, S., "Corrected Boundary Integral Equations in Planar Thermoelastoplasticity," Int. Jou. Sol. Struc., 13, pp. 331-335, 1977.

54. Kumar, V., and Mukherjee, S., "A Boundary Integral Formulation for Time-Dependent Inelastic Deformation in Materials," Int. Jou. Mech. Sci., 19, pp. 713-724, 1977.

55. Banerjee, P. K., and Mustce, G. G., "The Boundary Element Method for Two dimensional Problems of Elastoplasticity," in RECENT ADVANCES IN BOUNDARY ELEMENT METHODS (Brebbia, C. A. Ed.), University of Southampton, Southampton, pp. 283-300, 1978.

56. Bui, H. D., "Some Remarks about the Formulation of Three Dimensional Thermoelastoplastic Problems by Integral Equations," Int. Jou. Sol. Struc., 14, pp. 935-939, 1978.

57. Telles, J. F. C., and Brebbia, C. A., "On the Application of the Boundary Element Method to Plasticity," Appl. Math. Model., 3, pp. 466-470, 1979.

58. Hartmann, F., "Elasto Statics," in PROGRESS IN BOUNDARY ELEMENT METHODS, Vol. 1 (Brebbia, C. A. Ed.), John Wiley and Sons, New York, pp.113-114, 1981

59. Crouch, S. L., and Starfield, A. M., BOUNDARY ELEMENT METHODS IN SOLID MECHANICS, George Allen and Unwin Ltd., London, pp. 122-123, 1983.

60. Roberts E., and Mendelson A., "Analysis of Plastic Thermal Stress and Strain in Finite Thin Plate of Strain-Hardening Material," National Aeronautics and Space Administration Report, Huntsville, Ala., NASA TN D-2206, pp. 3-8, 1964.

61. Wetzler, F. U., "Digital Imaging Technology: Applications Are Expanding Everywhere," SPIE Opt. Eng. Reports, No. 48, pp. 3a-5a, Dec., 1987.

62. Chen, T. C., "Application of Digital Image Processing and Computer Graphics Techniques in Photomechanics," Ph.d. Dissertation, University of Florida, Gainesville, 1985.

63. Chen, T. C., and Taylor, C. E., "Computerized Fringe Analysis in Photomechanics," accepted for publication in Experimental Mechanics.

64. Burger, C. P, "Automated Moire' and Photoelastic Analysis with Digital Image Processing," PROC. 1984 SEM FALL CONF. ON EXP. MECH., Milwaukee, Wisc., 1984.

65. Robinson, D. W., "Automatic Fringe Analysis With a Computer Image-Processing System," Appl. Opt., 22, pp. 2169-2176, 1983.

66. Chu, T. C. , "Digital Correlation Method in
     Experimental Mechanics," Ph.d. Dissertation, University
     of South Carolina, Columbia, 1982.

67. Chu, T. C., Ranson, W. F., Sutton, M. A., and Peters,
     W. H., "Applications of Digital-Image-Correlation
     Techniques to Experimental Mechanics," Exp. Mech., 25,
     pp. 232-244, 1985.

68. Sutton, M. A., Wolters, W. J., Peters, W. H., Ranson,
     W. F., and McNeil, S. R., "Determination of
     Displacements Using an Improved Digital Correlation
     Method," Image and Vision Comp., pp. 133-139, 1983.

69. Fail, W. F., and Taylor, C. E., "An Application of
     Pattern Mapping to Plane Motion," unpublished.

70. Rosenfeld, A., and Davis, L. S., "Image Segmentation
     and Image Models," Proc. IEEE, 67, pp. 764-772, 1979

71. Fu, K. S., and Mui, J. K., " A Survey on Image
     Segmentation," Pat. Rec., 13, pp. 3-16, 1981.

72. Haralick, R. M., and Shapiro, L. G., "Image
     Segmentation Techniques," Comp. Vis., Graphics and Im.
     Pr., 29, pp. 100-132, 1985.

73. Hal, E. L., COMPUTER IMAGE PROCESSING AND RECOGNITION,
     Academic Press, New York, pp. 468-553, 1979.

74. Rosenfeld, A., "Image Analysis: Problems, Progress and
     Prospects," Pat. Rec., 17, pp. 3-12, 1984.

75. Mantas, J. "Methodologies in Pattern Recognition and
     Image Analysis-A Brief Survey," Pat. Rec., 20, pp. 1-6,
     1987.

76. Nagel, H. H., "Analysis Techniques for Image
     Sequences," PROC. 4th INT. JOINT CONF. ON PAT. REC.,
     Kyoto, pp. 186-211, 1978.

77. Gonzalez, R. C., and Wintz, P, DIGITAL IMAGE
     PROCESSING, Addison-Wesley Publ. Co., London, pp. 1-35,
     1977.

78. Tian, Q., and Huhns, M. N., "Algorithms for Subpixel
     Registration," Comp. Vis., Graphics and Im. Pr., 35,
     pp. 220-233, 1986.

79. Schreiber W. F., "Transition Between Continuous and Discrete Representations of Images:A Perceptual Approach," IEEE Trans. on Pat. Anal. and Mech. Int., pp. 178-186, 1985.

80. Rosenfeld, A., and Kak, C., DIGITAL PICTURE PROCESSING, Vol. 1, Academic Press, New York, pp. 214-250, 1982.

81. Boreman, G. D., "Fourier Spectrum Techniques for Characterization of Spatial Noise in Imaging Arrays, Opt. Eng., 26, No. 10, pp. 985-991, 1987.

82. Colquit, L., Bluzzer, N., and Mckee, R., "Charge Partition Noise in Charge-Couple Devices," Opt. Eng., 26, No. 10, pp. 992-998.

83. Jenkins, F. A., and White, H. E., FUNDAMENTALS OF OPTICS, McGraw-Hill, New York, pp. 149-182, 1976.

84. IVG-128 VIDEO ACQUISITION AND DISPLAY BOARD USERS MANUAL, Datacube, Inc., Peabody, Mass., 1987.

85. Merelli, D., Mussio, P., and Padula, M., "An Approach to the Definition, Description, and Extraction of Structures in Binary Digital Images," Comp. Vis., Graphics and IM. Pr., 31, pp. 19-49, 1985.

86. Lunscher, W. H. H., and Beddoes, M. P., "Fast Binary-Image Boundary Extraction," Comp. Vis., Graphics and Im. Pr., 38, pp. 229-257, 1987.

87. Wezska, J. S., "A Survey of Threshold Selection Techniques," Comp. Graph. and Im. Pr., 7, pp. 259-265, 1978.

88. Rosenfeld, A., and Kak, A, DIGITAL PICTURE PROCESSING, Vol. 2, Academic Press, New York, pp. 191-240, 1982

89. Susuki, S., and Abe, K., "Topological Structural Analysis of Digitized Binary Images by Border Following," Comp. Vis., Graphics and Im. Pr., 30, pp. 32-46, 1985.

90. Fu, K. S, DIGITAL PATTERN RECOGNITION, Springer-Verlag, New York, pp. 1-13, 1980.

91. Simon, J. C., "Recent Progress To Formal Approach of Pattern Recognition and Scene Analysis," Pat. Rec., 10, pp. 200-210, 1987.

92. Gonzalez, R. C., and Thomason, M. G., SYNTACTIC PATTERN RECOGNITION, Addison-Wesley Publ. Co., London, pp. 14-18, 1978.

93. Martin, W. N., and Aggarwal J. K.,, "Dynamic Scene Analysis," Comp. Graph. and Im. Pr., 7, pp. 356-374, 1978.

94. Eisenberg, M. A., INTRODUCTION TO THE MECHANICS OF SOLIDS, Addison-Wesley Pub. Co., Reading, Mass., pp. 128-130, 1980.

95. Theocaris, P. S., and Markedos, E., "Elastic Plastic Analysis of Perforated Thin Strips of a Strain Hardening Material," Jou. Mech. Phys. Solids, 12, pp. 377-390, 1964.

96. Kohnke, P. C., ANSYS, ENGINEERING ANALYSIS SYSTEM THEORETICAL MANUAL, Swanson Analysis Systems, Inc., Houston, Pa., pp. 4.0.1-4.1.33, 1983.

97. Zienkiewicz, O. C., THE FINITE ELEMENT METHOD, McGraw-Hill Book Co., London., pp. 469-471, 1977.

98. Ford, H., and Lianis, G., "Plastic Yielding of Notched Strips Under Conditions of Plane Stress," ZAMP, 8, pp.360-382, 1957.

99. Drucker, D. C., "On Obtaining Plane Strain or Plane Stress Conditions in Plasticity," PROC. OF THE 2nd U.S. NAT. CONG. OF APPL. MECH., ASME, pp.485-488, 1955.

100. Findley, W. N., and Drucker, D. C., "An Experimental Study of Plastic Straining of Notched Bars," JAM, 32, pp. 493-503, 1965.

101. Nayak, G. C., and Zienkiewicz, O. C., "Elasto-Plastic Stress Analysis. A Generalization for Various Constitutive Relations Including Strain Softening," Inter. Jou. Num. Meth., 5, pp. 113-135, 1972.